A perturbation approach to understanding the effects of turbulence on frontogenesis

Abigail S. Bodner[1,†]**, Baylor Fox-Kemper**[1]**, Luke P. Van Roekel**[2]**, James C. McWilliams**[3] **and Peter P. Sullivan**[4]

[1]Department of Earth, Environmental and Planetary Sciences, Brown University, Providence, RI 02912, USA

[2]Theoretical Division, Fluid Dynamics and Solid Mechanics, Los Alamos National Laboratory, Los Alamos, NM 87545, USA

[3]Department of Atmospheric and Oceanic Sciences, University of California, Los Angeles, CA 90095-1565, USA

[4]National Center for Atmospheric Research, Boulder, CO 80307-3000, USA

Ocean fronts are an important submesoscale feature, yet frontogenesis theory often neglects turbulence – even parameterized turbulence – leaving theory lacking in comparison with observations and models. A perturbation analysis is used to include the effects of eddy viscosity and diffusivity as a first-order correction to existing strain-induced inviscid, adiabatic frontogenesis theory. A modified solution is obtained by using potential vorticity and surface conditions to quantify turbulent fluxes. It is found that horizontal viscosity and diffusivity tend to be readily frontolytic – reducing frontal tendency to negative values under weakly non-conservative perturbations and opposing or reversing front sharpening, whereas vertical viscosity and diffusivity tend to only weaken frontogenesis by slowing the rate of sharpening of the front even under strong perturbations. During late frontogenesis, vertical diffusivity enhances the rate of frontogenesis, although perturbation theory may be inaccurate at this stage. Surface quasi-geostrophic theory – neglecting all injected interior potential vorticity – is able to describe the first-order correction to the along-front velocity and ageostrophic overturning circulation in most cases. Furthermore, local conditions near the front maximum are sufficient to reconstruct the modified solution of both these fields.

Key words: turbulent mixing, ocean processes, quasi-geostrophic flows

1. Introduction

The vast role of the ocean in the climate system spans from global processes such as water mass transport, sea level and heat content changes, to small-scale processes such as mixing heat, momentum and air–sea interactions (Siedler *et al.* 2013). It is common practice to partition the ocean into different time and length scales, as each have unique dynamical, statistical and energetic properties. The large-scale flow

† Email address for correspondence: abigail_bodner@brown.edu

is related to smaller-scale flows by transfer of energy between the scales, down to turbulence and the dissipative scales (e.g. Capet *et al.* 2008*b*; Ferrari & Wunsch 2009; Molemaker, McWilliams & Capet 2010; Callies *et al.* 2016). Mesoscale eddies span as large as hundreds of kilometres in horizontal length and months in time evolution, and tend to merge, transferring kinetic energy from smaller scales to the larger scales (inverse cascade), and so do not provide an easy route to dissipation (Ferrari & Wunsch 2009), except through intermittent interactions with boundary layers (Pearson & Fox-Kemper 2018). Consequently, submesoscale currents are thought to be a key component in the forward energy cascade in the ocean (see McWilliams (2016), and references therein). They span the range of 0.1–10 km in horizontal scale, 0.01–1 km in vertical scale and hours to days in time evolution. Because of the fast time scale, submesoscales respond faster to atmospheric forcing and play an important role in atmosphere–ocean interactions in the mixed layer (e.g. Bachman *et al.* 2017; Renault, McWilliams & Gula 2018). However, for these exact reasons, it has also been challenging to study submesoscale currents, since they are small and impermanent, requiring new strategies for ship surveys, satellite detection and global climate models. Submesoscale length and time scales, together with typical mixed layer stratification and instabilities, complicate the theoretical study of submesoscale dynamics (McWilliams 2016).

Fronts are an important and ubiquitous submesoscale feature of the upper ocean mixed layer. They are characterized by elongated sharp horizontal density gradients, and an ageostrophic overturning circulation in the interior, working to restore stratification and thermal wind balance, as mixing and strain alter the front. Due to the vertical properties of the ageostrophic overturning circulation, fronts are thought to play an important role in transporting tracers and supplying essential nutrients to marine biology (Mahadevan & Archer 2000; Taylor & Ferrari 2011; Mahadevan 2016; Smith, Hamlington & Fox-Kemper 2016; Olita *et al.* 2017). The ageostrophic overturning circulation has also recently been shown to be associated with the formation of gravity currents (Pham & Sarkar 2018).

The classic inviscid, adiabatic theory (Hoskins & Bretherton 1972; Hoskins 1982) of frontal formation, also referred to as frontogenesis, predicts that the cross-frontal scale becomes infinitely thin in finite time. This unphysical outcome does not comply with observations, both in the ocean and atmosphere (e.g. Bond & Fleagle 1985; Pollard & Regier 1992). Frontogenesis occurs in the ocean mixed layer where stratification may be complex, especially including the mixed layer base and connected upper pycnocline, and where the ocean surface is subject to atmospheric forcing by winds and thermal variations, waves and wave breaking, as well as incoming and outgoing radiative energy at short and long wavelengths. Thus, a variety of mixed layer instabilities or forced turbulent mixing affects fronts, many at a scale consistent with the width of observed fronts (Sullivan & McWilliams 2018). However, no scaling law or uniform understanding of how arrest happens over a variety of turbulent conditions exists, and present submesoscale parameterizations need such a scaling (Fox-Kemper *et al.* 2011).

As fronts involve both density and velocity gradients, there are potential roles for both turbulent momentum fluxes (usually simplified here as eddy viscosity) and turbulent heat fluxes (usually simplified here as eddy diffusivity). It is not well understood what kinds of turbulent fluxes may halt frontogenesis and at what scale, and what kinds enhance it and at what rate. For example, vertical mixing has been shown to be important for frontal formation (e.g. Thompson 2000; Nagai, Tandon & Rudnick 2006), whereas horizontal mixing is thought to play a role in the arrest

process (Sullivan & McWilliams 2018). Boundary layer mixing, specifically vertical momentum flux, has also been shown to incite frontogenesis through a process called turbulent thermal wind (McWilliams *et al.* 2015).

Much of the original theory of fronts was developed for the atmosphere, where they are critical for the understanding and prediction of weather. For example, a number of atmospheric studies (Nakamura & Held 1989; Cooper, Thorpe & Bishop 1992; Nakamura 1994; Xu, Gu & Gao 1998) study frictional potential vorticity (PV) injection, boundary conditions and nonlinear evolution in an evolving Eady (1949) wave, but they are simulation based while the theoretical perturbation approach taken here distinguishes the different viscous and diffusive contributions and boundary condition effects plainly. Rotunno, Skamarock & Snyder (1994) examine differences between the perfect semi-geostrophic equations and the primitive (effectively, the hydrostatic, Boussinesq) equations, noting that both dissipative terms and non-semi-geostrophic effects contribute. However, our target application is that of fully turbulent, non-hydrostatic, Boussinesq arrest, of the kind studied using large eddy simulations in Suzuki *et al.* (2016), Sullivan & McWilliams (2018) and subsequent studies, where non-hydrostatic boundary layer turbulence arrests frontogenesis within the upper ocean boundary layer. Håkansson (2002) illustrates how sensitive the atmospheric application is to the details of vertical friction and diffusivity. The oceanic application requires a still broader consideration of the kinds of turbulence that are possibly significant. While here the theory is illustrated with simple parameterizations of horizontal and vertical eddy diffusivities. Directly comparable to the past atmospheric studies, the approach presented here is readily extended to address the submesoscale (Fox-Kemper *et al.* 2011; Bachman *et al.* 2017) and Langmuir (Li *et al.* 2019) turbulence found to dominate oceanic boundary layer turbulence.

In this study, we present an analytic method based on perturbation analysis to account for the effects of modest turbulent fluxes on frontal formation. While constant eddy diffusivity and viscosity are utilized as concrete examples here, the approach is easily generalized to other more realistic turbulence closures or to large eddy simulation diagnostic analysis (an ongoing analysis will be reported soon). A complementary diagnostic decomposition approach has recently been proposed (McWilliams 2017), emphasizing the attribution of causes of frontogenesis to their effects. Here, an asymptotic approach is taken rather than a dynamical decomposition, illuminating different aspects of frontogenesis. In § 2 we review classic frontogenesis theory, present our asymptotic method in § 2.2 and the closed equation set of the modified solution, based on potential vorticity fluxes and boundary conditions, in §§ 2.3 and 2.4. Results are discussed in § 3, together with an analysis concerning localized approximations in §§ 3.1 and 3.2. Lastly, we conclude in § 4, followed by an outline for future work.

2. Theory and methods

The mathematical inviscid, adiabatic framework of strain-induced frontogenesis (Hoskins & Bretherton 1972; Hoskins 1982; Shakespeare & Taylor 2013) describes the formation of fronts when strained by a geostrophically balanced strain flow, such as mesoscale eddies (or synoptic weather in the atmospheric case). Shakespeare & Taylor (2013) (hereafter ST13) generalized the mathematical framework by Hoskins & Bretherton (1972) (hereafter HB72), to include fronts generated by an unbalanced flow. We follow the formulation presented in ST13 for a rotating fluid in Cartesian

coordinates in an incompressible, hydrostatic, Boussinesq flow on an untilted f-plane. In the limit of HB72, the equations reduce to the semi-geostrophic equations suited for describing the early stages of strain-induced frontogenesis. Eddy viscosity and diffusivity are added as new forcing terms, but otherwise this treatment and notation follows ST13.

The velocity and pressure terms are written as

$$\left.\begin{aligned} U = \bar{U} + u(x,z,t) = -\alpha x + u(x,z,t), \\ V = \bar{V} + v(x,z,t) = \alpha y + v(x,z,t), \\ W = 0 + w(x,z,t), \\ P = \bar{P} + p(x,z,t) = \rho_0\left[-\alpha^2\frac{(x^2+y^2)}{2} + f\alpha xy\right] + p(x,z,t), \\ B = 0 + b(x,z,t), \end{aligned}\right\} \quad (2.1)$$

where $\bar{U}$, $\bar{V}$, $\bar{P}$ are the background balanced, horizontal large-scale deformation fields and the associated pressure field respectively. The reference density is ρ_0, f is the Coriolis parameter and u, v, w, p, b are the laminar frontogenetic velocity, pressure and buoyancy fields. As appropriate for a mixed layer, upper ocean problem, weak background buoyancy stratification is assumed, so the background pressure field can be thought to occur primarily by sea surface height anomalies. The laminar frontogenetic fields are assumed to be nearly independent of the along-front direction y, so only $\bar{V}$ and $\bar{P}$ vary in y. The strain rate α is taken as a constant, an approximation valid when α represents much larger-scale features, such as mesoscale eddies, that do not vary over the confluence region of the submesoscale front in question. Furthermore, the semi-geostrophic approximation requires that $\alpha/f \ll 1$, which can also be described as a small Rossby number approximation. Note that y-invariance presumes that the laminar frontogenetic variables represent laminar perturbations to the background flow. All turbulent contributions will be assumed to be scale separated from these laminar flows, and thus treated via parameterization: here eddy viscosity and diffusivity are the explicit parameterization forms carried through the analysis, although generalizations are readily handled with the same methodology. To review, the flow is decomposed as a sum of background (capital letters), laminar frontogenetic (lower case) and turbulent (parameterized so not explicitly part of u, v, w, b, p, and either frontogenetic or frontolytic) pieces.

It is useful to introduce a vector streamfunction, with a geostrophic (vertical) component Φ (sometimes called 'velocity potential'), and an ageostrophic (along-front) component Ψ. The geostrophic streamfunction component is related to the pressure and horizontal geostrophic velocities by dividing into background and laminar frontogenetic contributions $\Phi = \bar{\phi} + \phi(x,z,t)$,

$$\bar{\phi} = \frac{\bar{P}}{\rho_0 f} + \alpha^2\frac{(x^2+y^2)}{2f} = \alpha xy, \quad \phi(x,z,t) = \frac{p(x,z,t)}{\rho_0 f}, \quad (2.2a,b)$$

$$\frac{\partial\bar{\phi}}{\partial y} = -\bar{U}, \quad \frac{\partial\bar{\phi}}{\partial x} = \bar{V}, \quad \frac{\partial\phi}{\partial y} = -u_g = 0, \quad \frac{\partial\phi}{\partial x} = v_g. \quad (2.3a\text{--}d)$$

While the ageostrophic, or 'overturning circulation', streamfunction component is related to the ageostrophic laminar frontogenetic velocities $\Psi = 0 + \psi(x,z,t)$,

$$\frac{\partial\psi}{\partial z} = u_a, \quad -\frac{\partial\psi}{\partial x} = w = w_a. \quad (2.4a,b)$$

Please note that to be consistent with ST13, we follow the left-hand rule definition for the streamfunction, rather than the right-hand rule as defined in HB72. Furthermore, here the term 'secondary' is avoided as a description of the overturning circulation, as it is easily confused with the order of the perturbation analysis. Likewise, the phrase 'laminar frontogenetic' is preferred over the more common 'perturbation' velocity because it is easily confused with terms involved in the perturbation method. As in HB72, the leading-order along-front laminar frontogenetic velocities are purely geostrophic ($v \equiv v_g$), and the cross-front laminar frontogenetic velocity is a combination of geostrophic and ageostrophic components ($u = u_g + u_a$). The background straining velocity is given by $\bar{\phi}$ alone.

Similar to ST13, the governing equations for the two-dimensional laminar frontogenetic response to the background flow can be expanded out from the definitions above, assuming hydrostatic, laminar flow. Here we include the novel addition of an eddy diffusive flux $F(b)$ and viscous flux $F(u)$, $F(v)$. For now, these are written in a form amenable to accommodate most present parameterizations, including spatial variation, non-local fluxes and tensor character (Large, McWilliams & Doney 1994; Griffies 1998; Fox-Kemper, Ferrari & Hallberg 2008; Bachman, Fox-Kemper & Bryan 2015; Bachman *et al.* 2017).

$$\frac{\mathrm{D}u}{\mathrm{D}t} - fv = \alpha u - \frac{1}{\rho_0}\frac{\partial p}{\partial x} + \nabla \cdot F(u), \tag{2.5a}$$

$$\frac{\mathrm{D}v}{\mathrm{D}t} + fu = -\alpha v + \nabla \cdot F(v), \tag{2.5b}$$

$$0 = b - \frac{1}{\rho_0}\frac{\partial p}{\partial z}, \tag{2.5c}$$

$$\frac{\mathrm{D}b}{\mathrm{D}t} = \nabla \cdot F(b), \tag{2.5d}$$

$$\frac{\partial u}{\partial x} + \frac{\partial w}{\partial z} = 0, \tag{2.5e}$$

where b is the buoyancy and from (2.5c) and (2.2) we have the relation

$$\frac{\partial \phi}{\partial z} = \frac{b}{f}. \tag{2.6}$$

The material derivative is defined as

$$\frac{\mathrm{D}}{\mathrm{D}t} \equiv \frac{\partial}{\partial t} + (u + \bar{U})\frac{\partial}{\partial x} + w\frac{\partial}{\partial z}. \tag{2.7}$$

Equation (2.5e) will be automatically satisfied if the streamfunctions ϕ and ψ are chosen as the prognostic variables instead of u, v, w.

For concreteness, we will assume in the following that the viscous and diffusive fluxes can be written as horizontal and vertical fluxes, assumed to be down gradient with constant viscosities and diffusivities

$$F(u) = \hat{x}v_H\frac{\partial u}{\partial x} + \hat{z}v_V\frac{\partial u}{\partial z}, \tag{2.8}$$

$$F(v) = \hat{x}v_H\frac{\partial v}{\partial x} + \hat{z}v_V\frac{\partial v}{\partial z}, \tag{2.9}$$

$$F(b) = \hat{x}\kappa_H \frac{\partial b}{\partial x} + \hat{z}\kappa_V \frac{\partial b}{\partial z}. \tag{2.10}$$

Consistent with assuming that the laminar fields do not vary in y, we assume that turbulent fluxes are statistically homogeneous in y and thus the $\hat{y}$ component can be ignored. One might be tempted to suggest that molecular viscosity and diffusivity might be used here, but we will soon see that asymptotic ordering demands an upper and a lower limit on Reynolds and Péclet number, so keep in mind that these terms are intended as turbulence parameterizations.

Within the mixed layer, these fluxes are assumed to be a direct result of turbulence, whereas in the very near-surface boundary they can be matched to applied wind shear (τ/ρ_0) and thermodynamic forcing (Q) via frictional and diabatic flux boundary conditions

$$\frac{\tau_x}{\rho_0} = \hat{z}\nu_V \frac{\partial u}{\partial z}, \tag{2.11a}$$

$$\frac{\tau_y}{\rho_0} = \hat{z}\nu_V \frac{\partial v}{\partial z}, \tag{2.11b}$$

$$Q = \hat{z}\kappa_V \frac{\partial b}{\partial z}. \tag{2.11c}$$

Penetrating solar fluxes can be accounted for, but are neglected here: all thermodynamic forcing is taken to be at the near surface.

2.1. *Dimensionless expressions*

Following ST13, we use the following scales to make the perturbation field equations dimensionless: the horizontal and vertical buoyancy gradients ($M^2 = \partial b/\partial y$ and $N^2 = \partial b/\partial z$, which is also the buoyancy frequency squared), the horizontal and vertical length scales (L, H) and the strain and Coriolis rate parameters (α, f). The dimensionless expressions for quantities of interest are given in table 1. As in ST13, the vertical dimensionless coordinate ranges from 0 to 1, 0 being the bottom of the mixed layer and 1 the surface. The cross-frontal coordinate is centred around the initial front maximum. We focus on the semi-geostrophic limit for the background and laminar frontogenetic velocities, which implies that the along-front velocity is purely geostrophic, and it is scaled accordingly. The cross-front horizontal velocity scaling is assumed to be consistent with the conversion of potential energy being the primary source for the frontal overturning kinetic energy $bH \sim U^2$ (e.g. Suzuki *et al.* 2016).

The dimensionless versions of (2.5b) and (2.5d) are, after reorganizing,

$$\left[\frac{\partial}{\partial t} + (Ro\,u + \gamma\bar{U})\frac{\partial}{\partial x} + Ro\,w\frac{\partial}{\partial z}\right]v = -\frac{1}{Ro}u - \gamma v + \left(\frac{Ro^2}{Re_H}\right)\frac{\partial^2 v}{\partial x^2} + \left(\frac{Ro^2}{Re_V}\right)\frac{\partial^2 v}{\partial z^2}, \tag{2.12a}$$

$$\left[\frac{\partial}{\partial t} + (Ro\,u + \gamma\bar{U})\frac{\partial}{\partial x} + Ro\,w\frac{\partial}{\partial z}\right]b = \left(\frac{Ro^2}{Pe_H}\right)\frac{\partial^2 b}{\partial x^2} + \left(\frac{Ro^2}{Pe_V}\right)\frac{\partial^2 b}{\partial z^2}. \tag{2.12b}$$

The dimensionless relations for ϕ, ψ, b and the velocities are

$$u = \frac{\partial\psi}{\partial z}, \quad \frac{\partial\phi}{\partial x} = v, \quad w = -\frac{\partial\psi}{\partial x}, \quad \frac{\partial\phi}{\partial z} = b. \tag{2.13a-d}$$

	Symbol	Scale
Buoyancy	b	M^2L
Geostrophic velocity	v	$\dfrac{HM^2}{f}$
Horizontal velocity	u	$\sqrt{M^2LH}$
Vertical velocity	w	$\sqrt{\dfrac{M^2H^3}{L}}$
Time	t	$\dfrac{1}{f}$
Background mean velocity	$\bar{U}$	αL
Rossby number	Ro	$\sqrt{\dfrac{M^2H}{f^2L}}$
Froude number	Fr	$\sqrt{\dfrac{M^2L}{N^2H}}$
Deformation ratio	γ	$\dfrac{\alpha}{f}$
Geostrophic streamfunction component	ϕ	M^2LH/f
Ageostrophic streamfunction component	ψ	$\sqrt{M^2LH^3}$
Horizontal turbulent Reynolds number (for horizontal eddy viscosity)	Re_H	$\dfrac{vL}{\nu}$
Vertical turbulent Reynolds number (for vertical eddy viscosity)	Re_V	$\dfrac{vH}{\nu}$
Horizontal turbulent Péclet number (for horizontal eddy diffusivity)	Pe_H	$\dfrac{vL}{\kappa}$
Vertical turbulent Péclet number (for vertical eddy diffusivity)	Pe_V	$\dfrac{vH}{\kappa}$

TABLE 1. Dimensionless expressions for quantities of interest following ST13 framework in the semi-geostrophic limit, which implies that the along-front velocity is purely geostrophic.

Based on these scalings, the error made in assuming v is geostrophic rather than using all of (2.5*a*) is $O(Ro)$, following the approach to the semi-geostrophic equations of Hoskins (1975). This assumption implies that if the turbulent flux terms are to contribute significantly when compared to the neglected ageostrophic terms in (2.5*a*), at least one of Re_H, Re_v, Pe_H or Pe_V should be smaller than Ro, which is a small parameter. Thus, at least one dissipative term must arise as an eddy parameterization, rather than through molecular values with Reynolds and Péclet numbers much larger than one. For the purposes of this paper, qualitative inferences of the effects of turbulent fluxes are sought, but in ongoing work diagnosing large eddy simulations, a comparison of the laminar frontogenetic velocities to resolved turbulence is being evaluated directly.

Following Hoskins (1982), we take the *z* derivative of (2.12*a*) and the *x* derivative of (2.12*b*), and using (2.13), reduce to one equation, representing the instantaneous

ageostrophic streamfunction governed by the strain field, geostrophic field and turbulent flux terms

$$\frac{\partial^2 \phi}{\partial z^2}\frac{\partial^2 \psi}{\partial x^2} - 2\frac{\partial^2 \phi}{\partial z \partial x}\frac{\partial^2 \psi}{\partial x \partial z} + \left(\frac{\partial^2 \phi}{\partial x^2} + \frac{1}{Ro^2}\right)\frac{\partial^2 \psi}{\partial z^2}$$
$$= -\frac{2\gamma}{Ro}\frac{\partial^2 \phi}{\partial x \partial z} + \left(\frac{Ro}{Re_H}\right)\frac{\partial^4 \phi}{\partial x^3 \partial z} + \left(\frac{Ro}{Re_V}\right)\frac{\partial^4 \phi}{\partial z^3 \partial x} - \left(\frac{Ro}{Pe_H}\right)\frac{\partial^4 \phi}{\partial x^3 \partial z} - \left(\frac{Ro}{Pe_V}\right)\frac{\partial^4 \phi}{\partial z^3 \partial x}.$$
$$(2.14)$$

In ST13 and HB72 an analytic solution is obtained by assuming zero or uniform PV everywhere in the domain. This class of solutions will be the zeroth-order starting point for the perturbation analysis here.

2.2. *Perturbation analysis*

For a small term ε we use perturbation analysis to account for the effects of turbulence. We construct the zeroth-order solution to contain all the leading-order laminar frontogenetic dynamics described in ST13 and HB72. Additionally, the background flow (i.e. $\bar{U}$, $\bar{V}$) is also part of the zeroth order, so for the inviscid, adiabatic, zeroth-order limit a zero PV valid solution exists.

$$\left.\begin{array}{r}U = \bar{U} + u = \varepsilon^0(\bar{U} + u^0) + \varepsilon^1 u^1 + O(\varepsilon^2), \\ V = \bar{V} + v = \varepsilon^0(\bar{V} + v^0) + \varepsilon^1 v^1 + O(\varepsilon^2), \\ W = w = \varepsilon^0 w^0 + \varepsilon^1 w^1 + O(\varepsilon^2), \\ \Phi = \bar{\phi} + \phi = \varepsilon^0(\bar{\phi} + \phi^0) + \varepsilon^1 \phi^1 + O(\varepsilon^2), \\ b = \varepsilon^0 b^0 + \varepsilon^1 b^1 + O(\varepsilon^2).\end{array}\right\} \quad (2.15)$$

At the first order, the effects of turbulence (2.8)–(2.10) and the associated surface forcing (2.11*a*)–(2.11*c*) on the laminar frontogenetic flow will be isolated and examined.

We will now study individually horizontal and vertical viscosity and diffusivity. For each case the small perturbation parameter ε is defined by

$$\left.\begin{array}{r}\varepsilon_{HV} = \dfrac{Ro}{Re_H} = Ek_H: \quad \text{Horizontal viscosity (HV)}, \\[2mm] \varepsilon_{VV} = \dfrac{Ro}{Re_V} = Ek_V: \quad \text{Vertical viscosity (VV)}, \\[2mm] \varepsilon_{HD} = \dfrac{Ro}{Pe_H} = \dfrac{Ek_H}{Pr_H}: \quad \text{Horizontal diffusivity (HD)}, \\[2mm] \varepsilon_{VD} = \dfrac{Ro}{Pe_V} = \dfrac{Ek_V}{Pr_V}: \quad \text{Vertical diffusivity (VD)},\end{array}\right\} \quad (2.16)$$

where $Ek_H = Ro/Re_H = \nu/fL^2$, $Ek_V = Ro/Re_V = \nu/fH^2$ and $Pr_H = \nu_H/\kappa_H$, $Pr_V = \nu_V/\kappa_V$ are the horizontal and vertical Ekman and Prandtl numbers. For small Ekman numbers and $O(1)$ Prandtl numbers, these terms are all expected to be small. However, depending on the details of the type of turbulence approximated, it may be expected that they may not be the same size. We proceed asymptotically by assuming they are all small and of equal order, and then after the asymptotic perturbation expansion we can choose to individually neglect them.

Using the eddy viscosity and diffusivity parameterizations (2.8)–(2.10), these small parameters appear before the terms of highest differential order. Hence, there will always be some small 'frictional sublayer' scale on which they are not small and they enlarge near the boundaries to satisfy the boundary conditions (2.11*a*)–(2.11*c*). A similarity or asymptotic matching solution may thus be more appropriate as an asymptotic approach in order to 'magnify' the sublayer region and examine potentially leading-order impacts outside the sublayer. However, other parameterizations of turbulence differ in differential order, e.g. a Newtonian drag as used in some eddy-damping boundary layer schemes (e.g. Parsons 1969; Fox-Kemper & Ferrari 2009) or Newtonian cooling as sometimes used in air–sea damping schemes (e.g. Dijkstra & Molemaker 1997) or linear drag as through parameterized Ekman layer pumping (Twigg & Bannon 1998; Boutle, Belcher & Plant 2015). Thus, the detailed asymptotics within the frictional boundary layer will be specific to the differential form of the parameterization – here eddy viscosity and diffusivity, but not generically those forms. Furthermore, the true ocean boundary has a wavy–frothy–bubbly sublayer for which there exist numerical approaches but not analytic ones. For these reasons, the effects of eddy viscosity and diffusivity in a specific frictional sublayer analysis are not the focus of this study. Rather, it is the intention here that the singular perturbation implied by neglecting these highest-derivative-order terms (i.e. as $\varepsilon \to 0$) be equivalent to the traditional solution of the classic inviscid, adiabatic frontogenesis theory, and may be used as a guide to later analyse realistic turbulent frontal simulations.

Thus, equation (2.14) is solved assuming an ansatz of regular perturbation analysis, and that the solution exists outside the frictional sublayer, affected only at first order by the turbulence there. We insert (2.15) above into (2.14) found in the previous section and separate by order of ε.

2.2.1. *Zeroth order: inviscid, adiabatic*

This order is the traditional frontogenesis regime, as studied by HB72 and ST13. Typically, a zero or uniform potential vorticity is assumed to arrive at a simpler solution. We will preserve this assumption for the zeroth order, but it will be revisited in the context of turbulent fluxes and potential vorticity anomalies and injection below. Additionally, to ensure consistency with the limitation of the Hoskins (1975) semi-geostrophic assumption and asymptotic theory, we confine this analysis to $\gamma = O(Ro^2)$ and $Ro < \varepsilon < O(Ro^{-2})$. However, as both Ro and ε must be small parameters, a tighter bound actually applies: $Ro < \varepsilon < 1$. The zeroth-order equation for the streamfunction, equation (2.14), equivalent to HB72, is

$$\frac{\partial^2 \phi^0}{\partial z^2}\frac{\partial^2 \psi^0}{\partial x^2} - 2\frac{\partial^2 \phi^0}{\partial z \partial x}\frac{\partial^2 \psi^0}{\partial x \partial z} + \left(\frac{\partial^2 \phi^0}{\partial x^2} + \frac{1}{Ro^2}\right)\frac{\partial^2 \psi^0}{\partial z^2} = -\frac{2\gamma}{Ro^2}\frac{\partial^2 \phi^0}{\partial x \partial z}. \qquad (2.17)$$

ST13 introduced a new coordinate system, similar to the geostrophic momentum coordinate in HB72,

$$X = e^{\alpha t}\left(x + \frac{v^0}{f}\right), \quad Z = z, \quad T = t. \qquad (2.18a-c)$$

This X coordinate is conserved for any value α and is referred to as the 'generalized momentum coordinate'. A similar expression for the vertical coordinate is desirable when the scale of gradient sharpening in the vertical is comparable to the horizontal

(e.g. McWilliams, Molemaker & Olafsdottir 2009). Here we assume frontal sharpening is dominated by the horizontal strain field, and thus strictly use the horizontal form of the generalized momentum coordinate. Note that since ST13 solve the inviscid non-diffusive case, this coordinate system is associated with the zeroth-order solution.

The dimensionless form of this coordinate system is

$$X = e^{\gamma T}(x + Ro\, v^0), \quad Z = z, \quad T = t. \qquad (2.19a-c)$$

In this new coordinate system, which tracks the Lagrangian displacements in x, the dimensionless material derivative reduces to

$$\frac{D}{Dt} = \frac{\partial}{\partial T} + Ro\, w^0 \frac{\partial}{\partial Z}. \qquad (2.20)$$

And the dimensionless Jacobian for this transformation is

$$J = e^{\gamma T}\left(1 - e^{\gamma T} Ro \frac{\partial v^0}{\partial X}\right)^{-1}. \qquad (2.21)$$

The solution for all the zeroth-order terms, assuming zero PV, are given in ST13. The buoyancy field is defined as

$$b^0(X, Z, T) = B_0(X) + Fr^{-2}Z + \Delta b^0(X, Z, T), \qquad (2.22)$$

where $B_0(X)$ is the initial imposed buoyancy field as a function of X, chosen to be $B_0(X) = \frac{1}{2}\text{erf}(X/\sqrt{2})$. For simplicity, we take the HB72 scenario (for which $v = v_g$) and the corresponding solution from ST13 is the following:

$$u^0 = -e^{\gamma T} Ro\, B_0'(X)(Ro\, w + (2Z-1)\gamma), \qquad (2.23a)$$

$$w^0 = Ro\, \gamma\, B_0''(X)Z(Z-1)e^{2\gamma T}\left(1 - Ro e^{\gamma T}\frac{\partial v^0}{\partial X}\right)^{-1}, \qquad (2.23b)$$

$$v^0 = e^{\gamma T} Ro\, B_0'(X)\left(Z - \tfrac{1}{2}\right). \qquad (2.23c)$$

Later, it will be useful when using the zeroth-order velocities to convert to coordinate system (2.19) where the velocities are written explicitly and have relatively simple expressions.

The criterion in ST13 for frontal singularity is that the transformation no longer holds, i.e. the inverse of the Jacobian vanishes ($J^{-1} = e^{-\gamma T} - Ro\, \partial v^0/\partial X$). This happens when $B_0'''(X_f) = 0$. For the HB72 case, the singularity forms at the critical time of $t = 19.8$, and the Eulerian location of this singularity is found to be

$$x_f = Ro\frac{1}{\sqrt{2\beta}}(X_f\, \beta + B_0'(X_f)), \qquad (2.24)$$

where $\beta = -B_0''(X) > 0$. Note that we expect x_f to appear in two locations: one at the surface, cold-side corner of the front in the mixed layer (x_{fs}) and the other at the base, warm-side corner of the front (x_{fb}).

Figure 1 illustrates the dynamical formation (in real space) of frontogenesis with the buoyancy field, and the emergence of the along-front velocity and cross-frontal overturning streamfunction. We follow ST13 in choosing $Ro = 0.4$, $\gamma = 0.1$ as
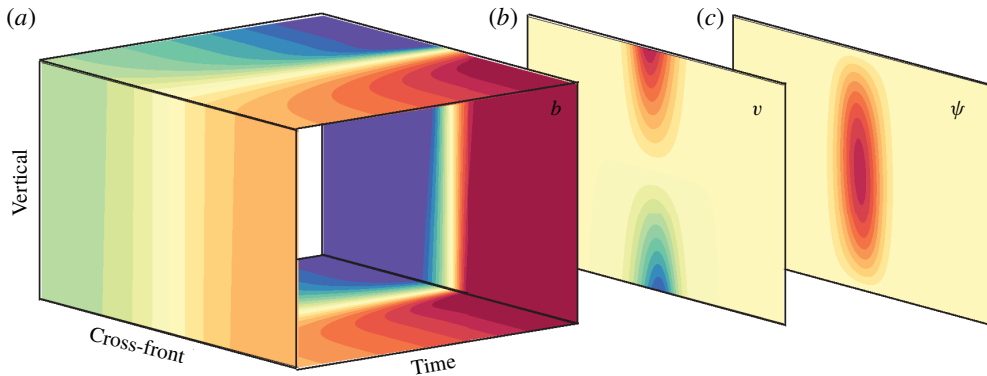
FIGURE 1. Frontal formation of the dimensionless zeroth-order buoyancy field (*a*), together with the cross-frontal planes showing the along-front velocity v (*b*), and overturning streamfunction ψ (*c*). The cross-frontal, vertical and time axes correspond to the dimensionless x, z and t axes respectively.
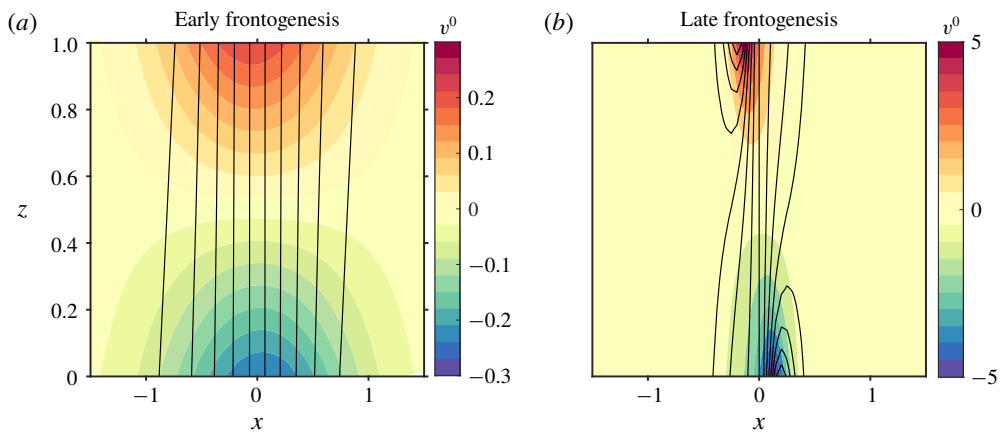

FIGURE 2. Cross-frontal profiles of the zeroth-order along-front velocity v^0 (shading) at two times defined as early frontogenesis ($t = 5$, *a*) and late frontogenesis ($t = 18$, *b*). Note the different colour bar axes. Superimposed in black contours is the buoyancy field, with intervals of 0.1 in non-dimensional units. Note the singularity developing during late frontogenesis. Here, x and z are the dimensionless cross-frontal and vertical axes, respectively, in real space.

an example for the HB72 case. As frontogenesis progresses, the imposed strain enhances the buoyancy gradient, which, through thermal wind balance, strengthens the along-front shear (figure 2). A useful diagnostic measure for frontal tendency is the Lagrangian evolution of the horizontal buoyancy gradient

$$T_b^0 = \frac{\mathrm{D}}{\mathrm{D}t} \frac{1}{2} \left(\frac{\partial b^0}{\partial x} \right)^2 \qquad (2.25)$$

(Hoskins 1982; McWilliams *et al.* 2015), shown in figure 3. Positive frontal tendency coincides with the largest buoyancy gradient, and in late frontogenesis a negative frontal tendency adjacent to the front maximum, contributes to the sharpening the front, eventually leading to singularity. An ageostrophic overturning circulation appears
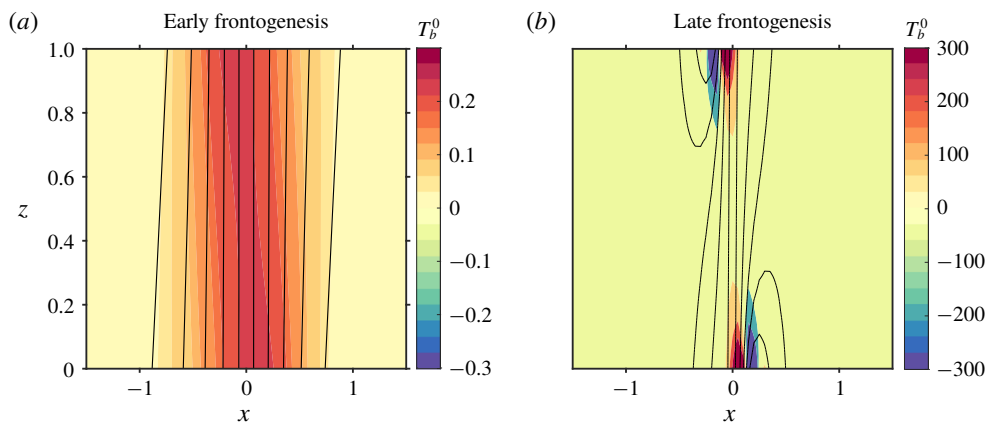
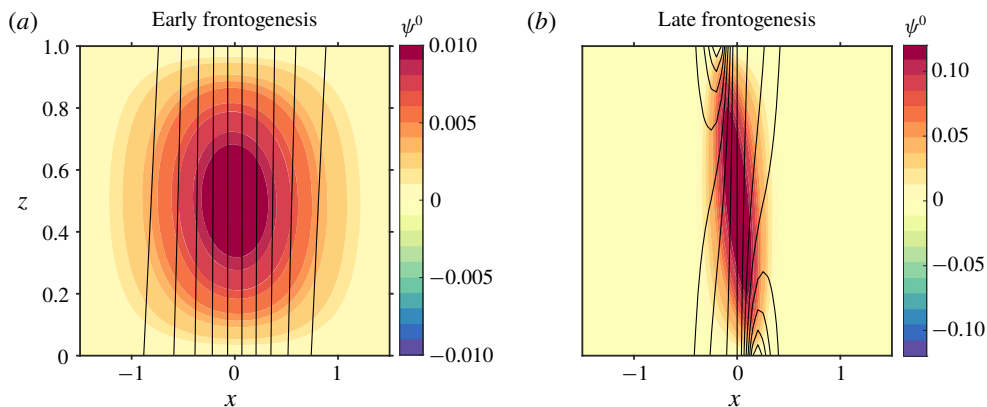FIGURE 3. Contours show buoyancy as in figure 2, shading shows the zeroth-order frontal tendency T_b^0.

FIGURE 4. Contours show buoyancy as in figure 2, shading shows the zeroth-order streamfunction ψ^0.

in the cross-frontal plane, attempting to re-stratify the front, further contributing to frontogenesis (figure 4). The positive overturning streamfunction in figure 4 indicates a counterclockwise overturning, which is in the direction to move buoyant water over dense and stratify the frontal region. However, as the frontal region is somewhat wider than the overturning, the upper left (upper, cold-side) and lower right (lower, warm-side) buoyancy gradients are concentrated more than other regions of the front. Illustrated in figures 2(b) and 4(b), as frontogenesis progresses, the ageostrophic streamfunction strengthens and narrows, and the along-front velocity gets pinched to two points at the top, cold-side corner and bottom, warm-side corner of the frontal region of the mixed layer, and the buoyancy gradient strengthens and isopycnals come closer together and tilt – especially in these two corners, consistent with the locations of maximum frontal tendency (figure 3). The zeroth-order solution continues to strengthen and narrow, and becomes singular at these two points within a finite time. In the following section, the first-order solution effects on this process are shown.

2.2.2. *First order: turbulent fluxes*

The first-order equation for the streamfunction given by (2.14) will be slightly different, depending on the type of forcing at hand

$$\frac{\partial^2 \phi^0}{\partial z^2}\frac{\partial^2 \psi^1}{\partial x^2} - 2\frac{\partial^2 \phi^0}{\partial z \partial x}\frac{\partial^2 \psi^1}{\partial x \partial z} + \left(\frac{\partial^2 \phi^0}{\partial x^2} + \frac{1}{Ro^2}\right)\frac{\partial^2 \psi^1}{\partial z^2}$$
$$= -\frac{\partial^2 \phi^1}{\partial x^2}\frac{\partial^2 \psi^0}{\partial z^2} + 2\frac{\partial^2 \phi^1}{\partial z \partial x}\frac{\partial^2 \psi^0}{\partial x \partial z} - \frac{\partial^2 \phi^1}{\partial z^2}\frac{\partial^2 \psi^0}{\partial x^2} - \frac{2\gamma}{Ro}\frac{\partial^2 \phi^1}{\partial x \partial z} + \mathcal{F}(\phi^0). \quad (2.26)$$

The different turbulent flux parameterizations arise as

$$\mathcal{F}(\phi^0) = \begin{cases} \dfrac{\partial^4 \phi^0}{\partial x^3 \partial z} & \text{(HV)}, \\[2mm] \dfrac{\partial^4 \phi^0}{\partial z^3 \partial x} & \text{(VV)}, \\[2mm] -\dfrac{\partial^4 \phi^0}{\partial x^3 \partial z} & \text{(HD)}, \\[2mm] -\dfrac{\partial^4 \phi^0}{\partial z^3 \partial x} & \text{(VD)}. \end{cases} \quad (2.27)$$

In our theoretical framework both surface boundary conditions and interior turbulent fluxes enter at the first order and are functions of zeroth-order terms. Thus (2.26) is an inhomogeneous (with turbulent flux divergences as forcing), second-order, linear (from perturbation method), partial differential equation (PDE) which is coupled for the unknown overturning and vertical streamfunction perturbations ψ^1, ϕ^1 with non-constant coefficients, which are known functions of the zeroth-order solution. In addition to the limitations on ε and *Ro*, this analysis is also restricted to times of early frontal formation, when $\psi^1 < O(1/\varepsilon)$ and the PDE (2.26) remains elliptic.

Note that the viscous terms are of opposite sign to the diffusive terms, but horizontal diffusivity and viscosity have the same operator, as do vertical diffusivity and viscosity. Although (2.27) suggests that diffusivity and viscosity may have opposite effects on frontal formation, an additional equation and boundary conditions that differ between viscosity and diffusivity are required in order to obtain the full uncoupled solutions for the first-order overturning and geostrophic streamfunction ϕ^1, ψ^1.

2.3. *Potential vorticity*

Potential vorticity, specifically Ertel PV, is a conserved quantity fundamental to geophysical fluid dynamics, and has historically been immensely useful in understanding oceanic and atmospheric dynamics (e.g. Gill 1982; Rhines 1986; Pedlosky 1987; Hoskins 1991; Salmon 1998; Kurgansky & Pisnichenko 2000). The PV is defined from the absolute vorticity ($\omega = f\boldsymbol{k} + \nabla \times \boldsymbol{u}$) and buoyancy gradient

$$q = (f\boldsymbol{k} + \nabla \times \boldsymbol{u}) \cdot \nabla b, \quad (2.28)$$

where $\boldsymbol{u} = (\bar{U} + u, \bar{V} + v, w)$ are the background and laminar velocity fields. Note that turbulent velocities are not included in this definition of PV, which is important in the interpretation of the eddy parameterizations. Since the zeroth-order PV is assumed to

be zero as in traditional frontogenesis theory, any PV in the perturbation system is associated with the first order and is a result of turbulent fluxes and boundary injection. The dimensionless first-order PV is

$$\frac{q^1}{Ro^2} = \frac{\partial v^1}{\partial x}\frac{\partial b^0}{\partial z} - 2\frac{\partial v^0}{\partial z}\frac{\partial b^1}{\partial x} + \left(\frac{1}{Ro^2} + \frac{\partial v^0}{\partial x}\right)\frac{\partial b^1}{\partial z}. \qquad (2.29)$$

Or in terms of ϕ^1,

$$\frac{q^1}{Ro^2} = \frac{\partial b^0}{\partial z}\frac{\partial^2 \phi^1}{\partial x^2} - 2\frac{\partial v^0}{\partial z}\frac{\partial^2 \phi^1}{\partial x \partial z} + \left(\frac{1}{Ro^2} + \frac{\partial v^0}{\partial x}\right)\frac{\partial^2 \phi^1}{\partial z^2}. \qquad (2.30)$$

The PV equation (2.30), like (2.26), is also an inhomogeneous (the forcing here is the non-zero PV), second-order, linear elliptic PDE for ϕ^1 with non-constant coefficients which are functions of the zeroth-order solution. As the zeroth-order solution is already known, then if given the strength of q^1, equation (2.30) can be inverted to find ϕ^1. From this, ψ^1 can be found using (2.26). So, if q^1 is known, then (2.30) and (2.26) are two coupled, linear PDEs in the unknowns ϕ^1, ψ^1.

The evolution of PV (which is just q^1 as the zeroth order has zero PV) is determined by frictional and diabatic forcing through the so-called J-equation, and can be written in terms of an advective term, a frictional flux term and diabatic flux term (Haynes & McIntyre 1987; Marshall & Nurser 1992; Thomas 2005; Benthuysen & Thomas 2012; Wenegrat *et al.* 2018):

$$\frac{\partial q}{\partial t} = -\boldsymbol{u} \cdot \boldsymbol{\nabla} q + (\boldsymbol{\nabla} \times \boldsymbol{D}_u) \cdot \boldsymbol{\nabla} b + \omega \cdot (\boldsymbol{\nabla} D_b), \qquad (2.31)$$

where $\boldsymbol{D}_u$ and D_b are the frictional and diabatic flux divergences.

Since the zeroth-order PV is uniform, the total PV equation reduces to the evolution of the first-order PV.

$$\frac{\partial q^1}{\partial t} = -\boldsymbol{u}^0 \cdot \boldsymbol{\nabla} q^1 + (\boldsymbol{\nabla} \times \boldsymbol{D}_u^1) \cdot \boldsymbol{\nabla} b^0 + \omega^0 \cdot (\boldsymbol{\nabla} D_b^1). \qquad (2.32)$$

In the asymptotic framework, the frictional and diabatic fluxes appear only in the first order and are functions only of known zeroth-order factors,

$$\boldsymbol{D}_u^1 = \boldsymbol{\nabla} \cdot F(v^0), \qquad (2.33a)$$
$$D_b^1 = \boldsymbol{\nabla} \cdot F(b^0). \qquad (2.33b)$$

Likewise, the advection of the first-order PV is only carried by the known zeroth-order velocity: $(\bar{U} + u^0, \bar{V} + v^0, w^0)$.

The non-dimensional form of this equation is

$$\frac{\partial q^1}{\partial t} = -\left[(Ro\, u^0 + \gamma \bar{U})\frac{\partial}{\partial x} + Ro\, w^0 \frac{\partial}{\partial z}\right] q^1 + \mathcal{D}(v^0, b^0), \qquad (2.34)$$

where the frictional and diabatic flux effects on PV have been collected into

$$
\mathcal{D}(v^0, b^0) = \begin{cases}
\dfrac{\partial b^0}{\partial x}\dfrac{\partial^3 v^0}{\partial x^2 \partial z} - \dfrac{\partial b^0}{\partial z}\dfrac{\partial^3 v^0}{\partial x^3} & \text{(HV)}, \\[2ex]
\dfrac{\partial b^0}{\partial x}\dfrac{\partial^3 v^0}{\partial z^3} - \dfrac{\partial b^0}{\partial z}\dfrac{\partial^3 v^0}{\partial z^2 \partial x} & \text{(VV)}, \\[2ex]
\dfrac{\partial v^0}{\partial z}\dfrac{\partial^3 b^0}{\partial x^3} - \dfrac{\partial v^0}{\partial x}\dfrac{\partial^3 b^0}{\partial x^2 \partial z} & \text{(HD)}, \\[2ex]
\dfrac{\partial v^0}{\partial z}\dfrac{\partial^3 b^0}{\partial z^2 \partial x} - \dfrac{\partial v^0}{\partial x}\dfrac{\partial^3 b^0}{\partial z^3} & \text{(VD)}.
\end{cases}
\tag{2.35}
$$

2.4. *Boundary conditions and first-order solution procedure*

To evaluate first-order solutions for each of the frictional forcing cases, equation (2.34) is integrated in time using the zeroth-order terms from (2.22) and (2.23a)–(2.23c). During integration, the first-order PV is calculated, advected and accumulated.

The first-order solution is next found, for every forcing case, by solving (2.26) and (2.30) using the PV resulting from (2.34). By integrating equations (2.5a) and (2.5d), the vertical boundary conditions are solved at each time. Explicitly, the vertical boundary conditions are calculated by following the evolution of the first-order buoyancy and cross-frontal velocity at the top and bottom boundaries, for each forcing case

$$
b^1 = \frac{\partial \phi^1}{\partial z}, \quad b^1|_{z=0,1} = \int_0^t [-\boldsymbol{u}^0 \cdot \nabla b^1 - \boldsymbol{u}^1 \cdot \nabla b^0 + \nabla \cdot F(b^0)]\Big|_{z=0,1} \, \mathrm{d}t, \tag{2.36a}
$$

$$
u^1 = \frac{\partial \psi^1}{\partial z}, \quad u^1|_{z=0,1} = \int_0^t [-\boldsymbol{u}^0 \cdot \nabla u^1 - \boldsymbol{u}^1 \cdot \nabla u^0 + \gamma u^1 + \nabla \cdot F(u^0)]\Big|_{z=0,1} \, \mathrm{d}t, \tag{2.36b}
$$

$$
q^1|_{z=0,1} = \left[Ro^2 \frac{\partial b^0}{\partial z}\frac{\partial^2 \phi^1}{\partial x^2} - 2Ro^2 \frac{\partial v^0}{\partial z}\frac{\partial^2 \phi^1}{\partial x \partial z} + \left(1 + Ro^2 \frac{\partial v^0}{\partial x}\right)\frac{\partial^2 \phi^1}{\partial z^2} \right]\Big|_{z=0,1}. \tag{2.36c}
$$

It is important to note that the fluxes producing PV in the preceding equations are surface turbulent fluxes associated with frontal formation. At this time we do not consider external surface forcing, such as wind stress, which has been shown to contribute additional interior PV (Thomas & Ferrari 2008).

The horizontal boundary conditions assume the laminar frontogenetic fields vanish in the horizontal, far from the front. Explicitly,

$$
v^1|_{x \to \pm\infty} = \frac{\partial \phi^1}{\partial x}\bigg|_{x \to \pm\infty} = 0, \tag{2.37a}
$$

$$
u^1|_{x \to \pm\infty} = \frac{\partial \psi^1}{\partial z}\bigg|_{x \to \pm\infty} = 0, \tag{2.37b}
$$

$$
q^1|_{x \to \pm\infty} = 0. \tag{2.37c}
$$

The initial conditions for all first-order terms, which include the PV, ψ^1 and ϕ^1 are zero, assuming turbulence and secondary circulations are negligible at $t = 0$ when the front is weak. More details on the numerical methods used to illustrate the results in the following section can be found in appendix A.
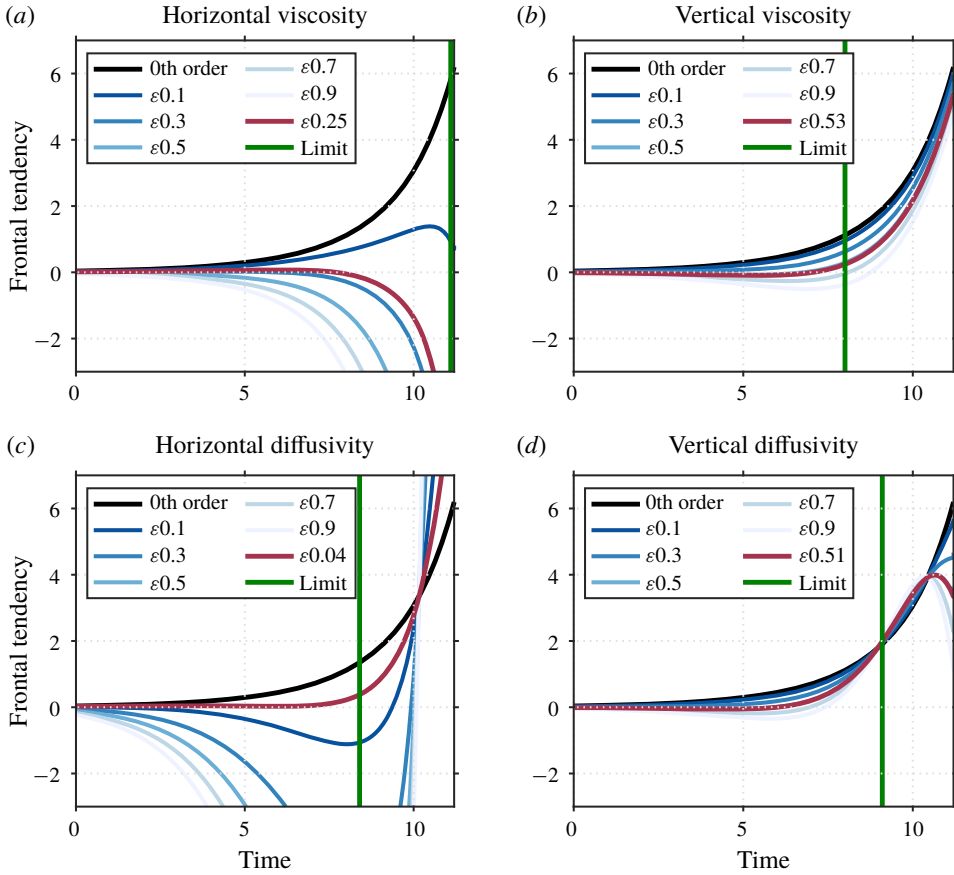
FIGURE 5. Total frontal tendency $T_b = T_b^0 + \varepsilon T_b^1$ for each of the forcing cases, over a variety of ε (shades of blue), evaluated at the surface, where the zeroth-order frontal tendency maximum (black) becomes infinitely strong. For each forcing case, the maroon line represents the ε for which $T_b = 0$. The green vertical line represents the time where the limit of the perturbation approach is reached for each forcing case: horizontal viscosity ($t = 11.1$), vertical viscosity ($t = 8$), horizontal diffusivity ($t = 8.4$), vertical diffusivity ($t = 9.1$).

3. Results

To quantify the effects turbulent fluxes may have on frontal formation, the first-order frontal tendency is a useful start, evaluated by

$$T_b^1 = \frac{D}{Dt_0}\left(\frac{\partial b^0}{\partial x}\frac{\partial b^1}{\partial x}\right) + \frac{D}{Dt_1}\frac{1}{2}\left(\frac{\partial b^0}{\partial x}\right)^2, \tag{3.1}$$

where subscripts on the Lagrangian derivative operator indicate the order of the advecting velocities. The total frontal tendency, i.e. $T_b = T_b^0 + \varepsilon T_b^1$, is sensitive to the choice of ε and the turbulent forcing at hand. Presented in figure 5 are the total frontal tendencies for each of the forcing cases, over a variety of ε (shades of blue), evaluated at the surface, where the zeroth-order frontal tendency maximum (black) becomes infinitely strong. For each forcing case, the maroon line represents the ε

for which $T_b = 0$. This is a major result of this study, as it implies that there exists a choice of parameters, for each turbulent forcing case, that is able to temporarily resist the strengthening of the front, i.e. lead to an arrest. It is important to note that ε is different for every forcing case, as well as the length of time for which it is able to sustain an arrest. However, the limitations of the perturbation theory are highlighted by the erratic behaviour of the solution at later times, a reminder that this theory is valid only for early frontal formation while higher-order corrections remain insignificant. In figure 5, a green vertical line is used to indicate when higher-order terms begin to rival leading-order terms – i.e. an estimate of the breakdown time of the perturbation method.

A closer look reveals that horizontal turbulent forcing cases share similar properties, as do the vertical. Both horizontal viscosity and diffusivity show a linear response in epsilon towards a weakening of the total frontal tendency, i.e. as ε increases, T_b becomes more negative. Additionally, the ε which enables an arrest is relatively small, only $\varepsilon = 0.25$ in the horizontal viscosity case and $\varepsilon = 0.04$ in the horizontal diffusivity case. Vertical viscosity and diffusivity also can reduce the rate at which frontal tendency grows, however larger values of ε are required to reach negative frontal tendency. During late frontogenesis (near time 10), larger values of vertical diffusivity enhance the rate of frontogenesis over the zeroth-order solution, with larger ε leading to faster frontal tendency (although this effect occurs after perturbation theory is estimated to remain formally accurate). To make early time frontal tendency negative, very large values of ε are needed with the vertical operators. Furthermore, larger values of the arrest ε are found in the vertical cases, where $\varepsilon = 0.53$ in the vertical viscosity case and $\varepsilon = 0.51$ in the vertical diffusivity case. Indeed, $Ro = 0.4 < \varepsilon < 1$ is required by the asymptotics, so much larger ε are not accessible consistently. By contrast, very small values of ε optimize arrest (as simulated in the perturbation theory) in the horizontal viscosity ($\varepsilon \approx 0.25$) and especially diffusivity ($\varepsilon \approx 0.04$) cases. The perturbation assumption of $Ro \sim \varepsilon$ does not apply for such small ε values, and these specific values are unlikely to be accurate (Barcilon 1998; Bender & Orszag 2013). However, even a small amount of horizontal diffusivity surely affects frontogenesis strongly. In practice, even small amounts of horizontal numerical viscosity and diffusivity will have a large impact on frontogenesis, consistent with other findings (see discussion in McWilliams *et al.* (2009)). Because numerical stability requires (horizontal) diffusivity and viscosity to scale with (horizontal) resolution, much higher horizontal resolution is required to properly capture frontogenesis numerically than one would naively expect based on assumed balances such as $Ro \sim \varepsilon$. Thus, recent oceanic large eddy simulations of frontogenesis (e.g. Suzuki *et al.* 2016; Sullivan & McWilliams 2018) are likely addressing a novel regime where horizontal fluxes may contribute unlike in coarser hydrostatic models. Likewise, the results here that vertical turbulent fluxes approach leading order to contribute to arrest – or even become frontogenetic as in the vertical diffusivity near time 10 – is likewise consistent with recent numerical analyses of the frontogenetic turbulent thermal wind effects.

To better understand the underlying dynamics of the possible arrest mechanism for each forcing case, we next examine the cross-frontal planes of the total frontal tendency ($T_b = T_b^0 + \varepsilon T_b^1$, figure 6), along-front velocity ($v = v^0 + \varepsilon v^1$, figure 7) and streamfunction ($\psi = \psi^0 + \varepsilon \psi^1$, figure 8). All figures are displayed at non-dimensional time $t = 5$, and with the appropriate arrest ε for each forcing case found in figure 5. Black ticks indicate the location of maximum zeroth-order frontal tendency corresponding to that measured in figure 5, and for the sense of where the front is
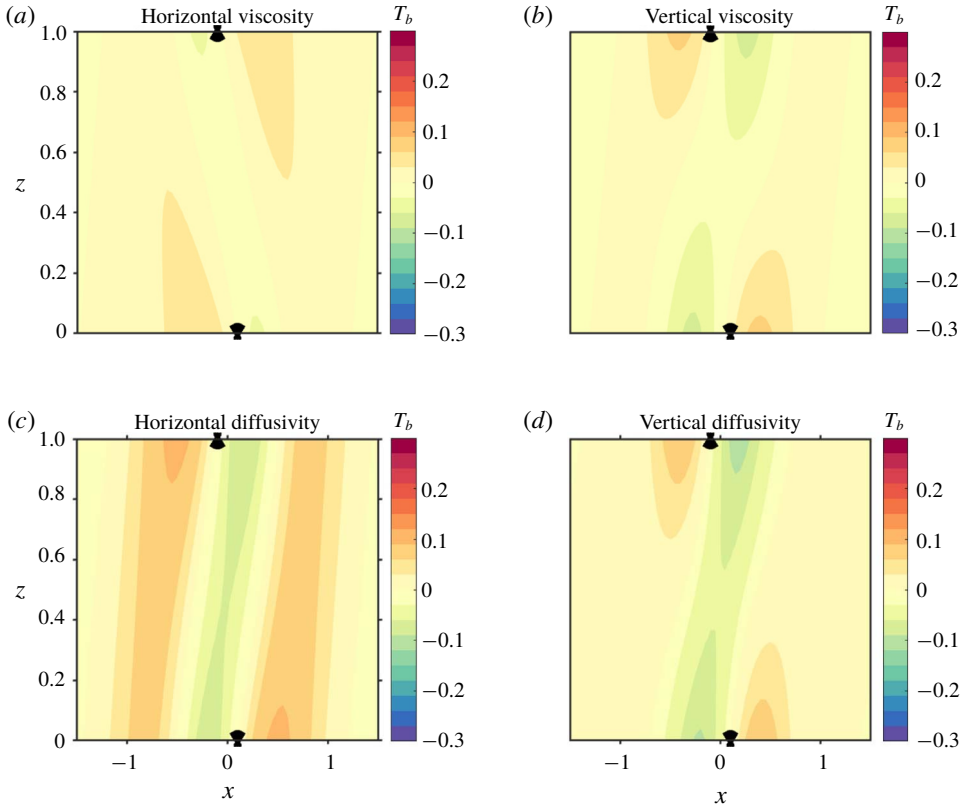
FIGURE 6. Cross-frontal plane of the total frontal tendency $T_b = T_b^0 + \varepsilon T_b^1$ during early frontogenesis ($t = 5$) with the appropriate arrest ε for each forcing case: horizontal viscosity ($\varepsilon = 0.25$), vertical viscosity ($\varepsilon = 0.53$), horizontal diffusivity ($\varepsilon = 0.04$), vertical diffusivity ($\varepsilon = 0.51$). Black ticks indicate the location of the maximum zeroth-order frontal tendency corresponding to that measured in figure 5 and for the sense of where the front is strongest.

strongest. All forcing cases exhibit zero total frontal tendency at the location of the zeroth-order maximum (figure 6), which is expected by choosing the arrest ε for each case. A demonstration of the arrest is also apparent, for each forcing case, in the spreading and weakening of the along-front velocity at the surface (figure 7).

However, in the zeroth-order solution illustrated in figures 2–4, the overturning streamfunction tended to focus the buoyancy gradients in two corner points, consistent with the locations of maximum frontal tendency, and where eventually frontal singularities first develop. In the perturbation solutions combined to first order in figures 6–8, the behaviour at these points is different depending on which turbulent forcing case is examined.

(i) Horizontal viscosity: the frontal tendency (figure 6) exhibits weak negative and positive signals adjacent to the zeroth-order frontal maximum, of opposite orientation to figure 3 during late frontogenesis. Furthermore, a negative streamfunction (figure 8) appears near the surface, right of the region of maximum zeroth-order frontal tendency, directing fluid and gradients away from
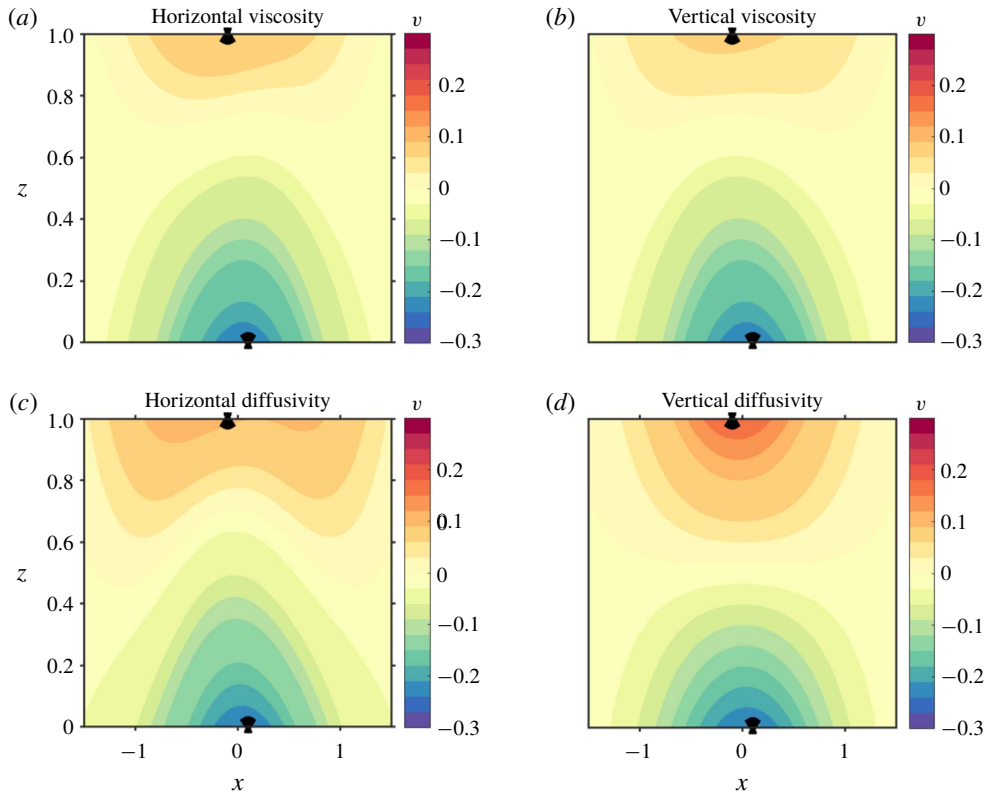
FIGURE 7. Same as in figure 6 for the total along-front velocity $v = v^0 + \varepsilon v^1$.

the front maximum. This supports the findings in figure 5, that the contribution of horizontal viscosity at the first order tends to weaken the front.

(ii) Vertical viscosity: although weaker in magnitude, the frontal tendency (figure 6) in this case is of similar orientation to the front maximum as in figure 3 during late frontogenesis. Here, a negative streamfunction (figure 8) appears near the surface as well, but in opposite configuration with respect to the front maximum when compared to the horizontal viscosity case, thus directing fluid and gradients to concentrate toward the region of maximum zeroth-order frontal tendency. Although, at time $t = 5$ the total frontal tendency is near zero, the flow indicates that vertical viscosity at the first order tends to enhance frontogenesis, consistent with results from previous studies.

(iii) Horizontal diffusivity: the along-front velocity is relatively widespread in figure 7 as compared with the other cases, even for a relatively small value of ε. The streamfunction (figure 8) similarly is widespread, however the streamfunction reverses sign for increased ε, directly opposing the zeroth-order streamfunction (not shown). Interestingly, the frontal tendency in this case (figure 5) does not resemble that of the horizontal viscosity case. Rather, it is of the same configuration as vertical viscosity and diffusivity, which may explain the acceleration found in figure 5 approaching the perturbation limit at time $t = 8.4$. However, horizontal diffusivity in figure 5 displays a weakening even for very
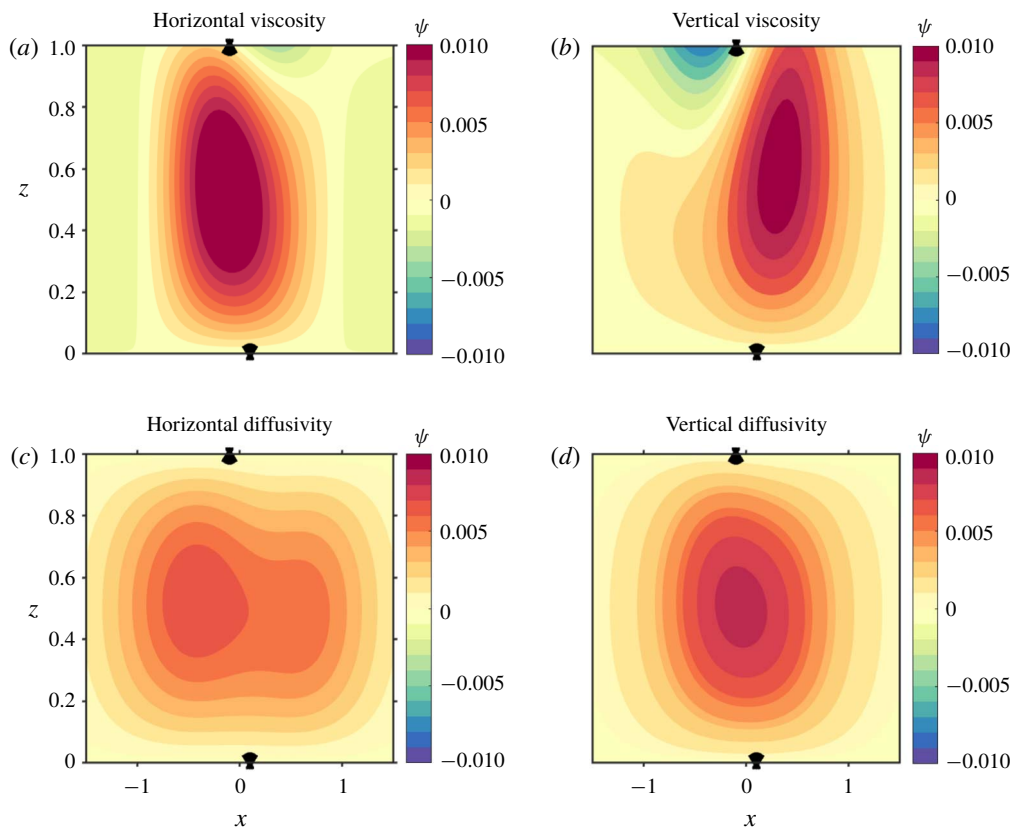
FIGURE 8. Same as in figure 6 for the total streamfunction $\psi = \psi^0 + \varepsilon \psi^1$.

small values of ε and thus, we conclude that horizontal diffusivity, similar to horizontal viscosity, has mostly frontolytic characteristics.

(iv) Vertical diffusivity: similar to the vertical viscosity case, the frontal tendency here (figure 6) exhibits the same configuration as in figure 3. However, the streamfunction (figure 8) displays a weak wider shape in the interior, yet is more concentrated near the surface. The streamfunction shape does not reveal much intuition regarding the effects of vertical viscosity on the flow field. For smaller ε, the streamfunction magnitude is stronger, and for larger ε more concentrated at the surface (not shown). Figure 5 shows that, as the perturbation limit is approached at time $t = 9.1$, the total frontal tendency for all values of ε accelerates and focuses at the zeroth-order value. The time this occurs is likely sensitive to parameters such as Ro and γ. We conclude that vertical diffusivity, similar to vertical viscosity, is frontogenetic based on the frontal tendency, yet not easily understood from the streamfunction flow field.

To summarize, the first-order solution is distinguished from the zeroth-order solution in two ways, by the computed interior PV and through the altered boundary conditions that arise at first order. The first-order solutions examined in this section are surprisingly complex in comparison to the simple reversal of signs in (2.35) – the solutions are not just mirror images because the surface boundary conditions for momentum and buoyancy are not simply related, even though the field equations are.

It is now natural to ask whether the solution is fully dependent on both or whether either the interior PV or the surface conditions dominates over the other.

3.1. *Surface quasi-geostrophy versus interior quasi-geostrophy*

In the mixed layer, surface quasi-geostrophic (SQG) dynamics (Lapeyre & Klein 2006; Lapeyre, Klein & Hua 2006) sometimes dominates over interior quasi-geostrophic (IQG) dynamics forced by anomalies in ocean interior PV (Klein *et al.* 2011), also called Charney (1971) QG dynamics (Bretherton 1966; Capet *et al.* 2008*a*; Stamper, Taylor & Fox-Kemper 2018). The IQG has been shown in some simulations to enhance frontogenesis over SQG-only upper ocean cases (Capet *et al.* 2016), and can nonetheless exhibit mesoscale strain-induced frontogenesis to some degree which is enhanced by submesoscales (Callies *et al.* 2016). The relative contributions of the SQG system are more easily detected by remote sensing (e.g. LaCasce & Mahadevan 2006; LaCasce & Wang 2015; Chavanne & Klein 2016).

In an SQG system, surface buoyancy anomalies are used to generate an active boundary condition, while the interior PV is taken to be uniform and inert (Blumen 1978). The full flow field is obtained by using the PV invertibility principle (Hoskins, McIntyre & Robertson 1985), with the active buoyancy field providing the boundary conditions for the inversion. In the IQG system, the boundary conditions are simplified by neglecting buoyancy anomalies and the flow dynamics is assumed to be driven solely by interior quasi-geostrophic PV anomalies (QGPV). Two interesting by-products of the perturbation analysis framework are that the first-order Ertel PV, as ordinarily used in the traditional frontogenesis literature, is locally equivalent to QGPV at that order, and that the impact of the first-order solution can be uniquely and completely decomposed into SQG effects and IQG effects (figures 9 and 10). Turbulent closures affect surface buoyancy quite differently from interior PV, so, are the effects on frontal formation by interior PV comparable to surface turbulent fluxes?

The PV in (2.30), together with the buoyancy boundary condition on ϕ in (2.36*a*) and (2.37*a*), can thus be constructed from a combination of the interior QGPV, which in isolation drives the IQG system, and added delta functions based on surface buoyancy to replace the buoyancy boundary condition (Bretherton 1966), which in isolation drive the SQG system (more details in appendix A). The surface delta boundary conditions are explicitly calculated by following the evolution of the first-order buoyancy and cross-frontal velocity at the surface, for each forcing case

$$b^1 = \frac{\partial \phi^1}{\partial z}, \quad b^1 = \int_0^t [-\boldsymbol{u}^0 \cdot \boldsymbol{\nabla} b^1 - \boldsymbol{u}^1 \cdot \boldsymbol{\nabla} b^0 + \boldsymbol{\nabla} \cdot F(b^0)] \delta(z - 0) \, \mathrm{d}t, \quad (3.2a)$$

$$u^1 = \frac{\partial \psi^1}{\partial z}, \quad u^1 = \int_0^t [-\boldsymbol{u}^0 \cdot \boldsymbol{\nabla} u^1 - \boldsymbol{u}^1 \cdot \boldsymbol{\nabla} u^0 + \gamma u^1 + \boldsymbol{\nabla} \cdot F(u^0)] \delta(z - 0) \, \mathrm{d}t. \quad (3.2b)$$

A delta function for the bottom boundary condition is used as well, although this has little effect on the end result. These are essentially identical to the full first-order boundary conditions (2.36*a*)–(2.36*b*).

Figures 9 and 10 show the cross-frontal planes of the first-order along-front velocity v^1 and streamfunction ψ^1 at time $t = 5$ for all forcing cases, calculated from the full system (*a*)–(*d*), the IQG system (*e*)–(*h*), the SQG system (*i*)–(*l*) and their sum (*q*)–(*t*). Panels (*m*)–(*p*) will be discussed in the following subsection.

To obtain the along-front velocity, we solve a linear PDE in ϕ^1, and thus expect the sum of the SQG and IQG systems to be similar to that of the full system. For
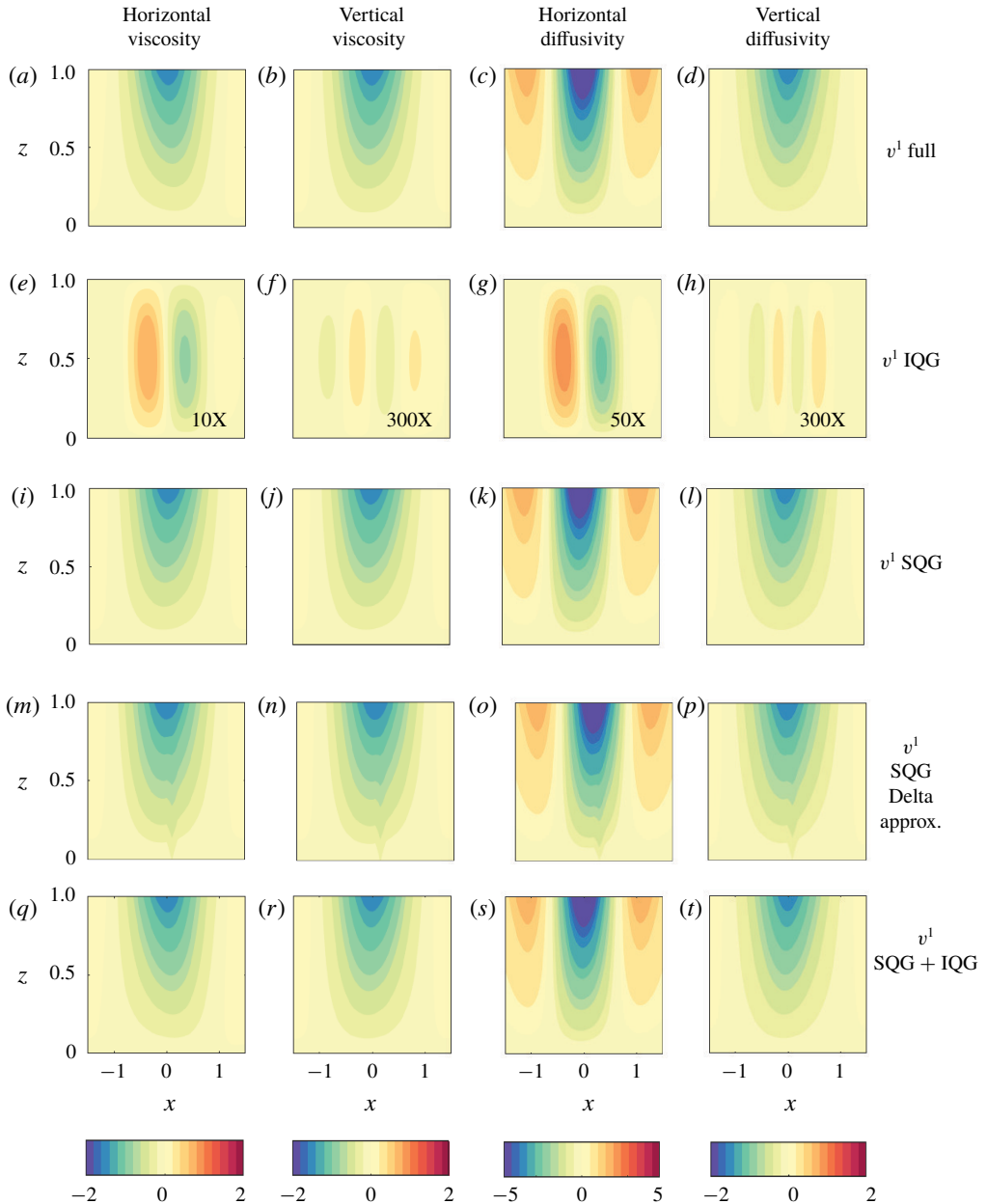
FIGURE 9. Cross-frontal planes of the first-order along-front velocity v^1 at time $t = 5$ for all forcing cases, calculated from the full system (a)–(d), the IQG system (e)–(h), the SQG system (i)–(l), the SQG system with a point source approximation (m)–(p) and the sum of the SQG and IQG systems (q)–(t). Note that for plotting purposes the IQG system is multiplied by a constant.

all forcing cases, the full and SQG systems in figure 9 are characterized by negative velocity, centred at the surface and decreasing with depth. On the other hand, the IQG system shows a significantly weaker velocity, with a dipole shape (or double dipole
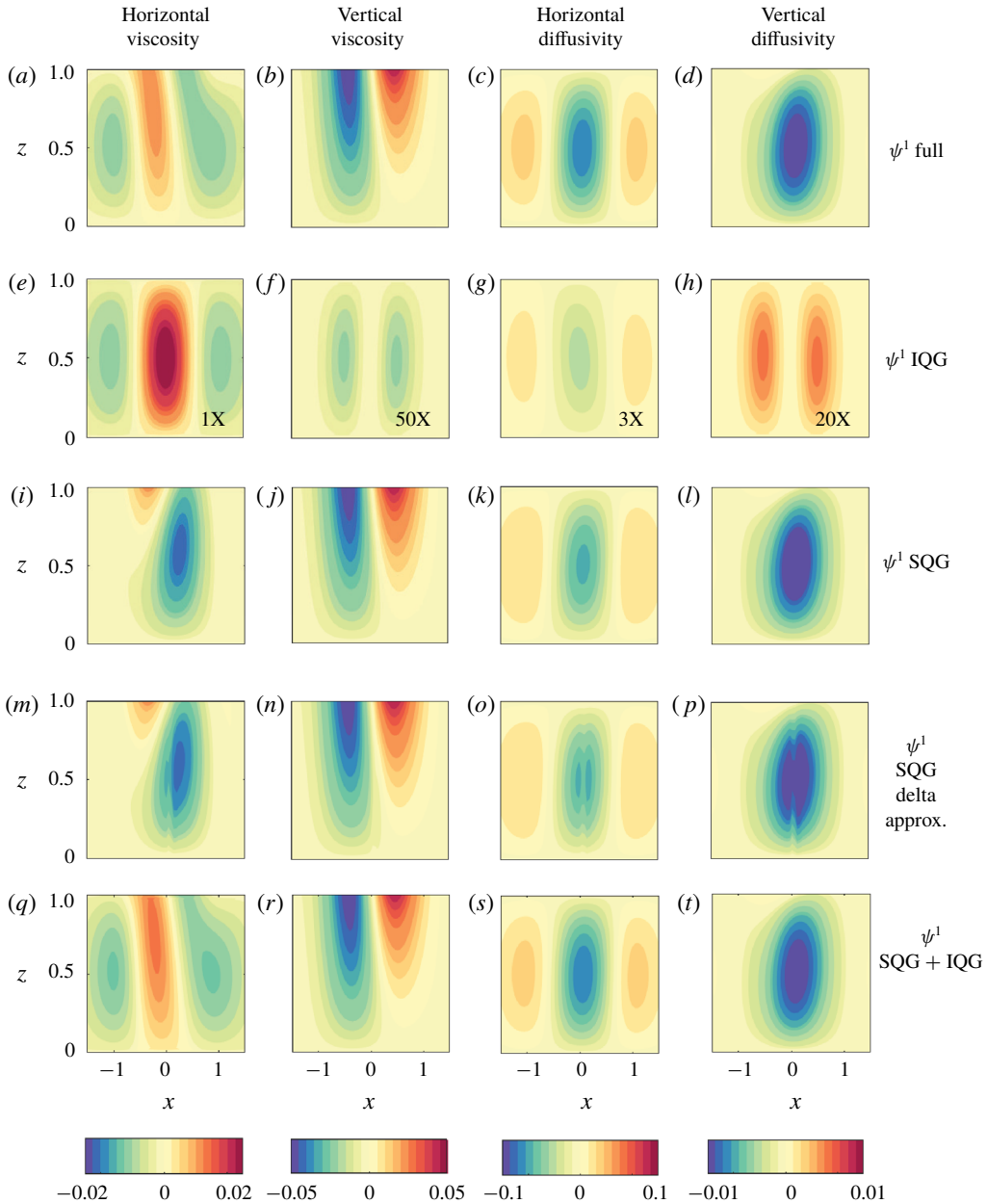
FIGURE 10. Same as in figure 9 for the first-order streamfunction ψ^1. Note that for plotting purposes also here the IQG system is multiplied by a constant.

in the vertical cases). Hence, for the along-front velocity, representing the geostrophic field, the SQG system appears to capture most elements of the complete solution.

Unlike the equation for ϕ^1, the streamfunction ψ^1 has a forcing term that cannot be easily attributed to SQG or IQG dynamics, as it is governed by zeroth-order terms. For illustration purposes, we divide this forcing term into surface and interior domains (more details in appendix A), and solve for the SQG and IQG systems

separately. The first-order streamfunction exhibits different behaviour for each forcing case in figure 10. The full solution for the horizontal and vertical viscosity cases is focused near the surface, whereas in the horizontal and vertical diffusivity cases the streamfunction is centred in the interior. Furthermore, unlike figure 9, the IQG system is comparable in magnitude in the horizontal cases, yet weaker in the vertical cases. The sum of the SQG and IQG systems is very similar to the complete system in all cases, however only in the horizontal viscosity case does the IQG system contribute significantly in the interior.

Thus, given surface turbulent fluxes, the first-order correction of the along-front velocity and geostrophic potential can be found to a good approximation merely from surface conditions, using SQG theory in this classic strain-induced frontogenesis case. The overturning streamfunction and ageostrophic field reveal a more complex dependency on interior fluxes, which by affecting interior PV, may be important for a complete solution below the surface. This implies that parameterizations that affect the surface buoyancy will have a larger impact on frontal structure than those that affect interior PV or the rate of PV injection.

3.2. *Point source surface quasi-geostrophy*

In the SQG framework, we followed Bretherton (1966), and used delta functions in z to replace the surface buoyancy boundary conditions. The success of this approach in capturing much of the full frontogenesis impacts on along-front velocity highlights the importance of surface buoyancy gradients. We now examine a further simplification of buoyancy that is severely focused in the horizontal direction as well to see how much of the effect is retained. During frontogenesis, the buoyancy has a sharp, and sharpening, gradient over the frontal domain. As the buoyancy singularity is approached, the cross-frontal buoyancy gradient $\partial b^1/\partial x$ may be approximated by a delta function in the cross-frontal direction, corresponding to the location of maximum frontal tendency, and buoyancy gradients elsewhere being neglected. Using this assumption, a simplified boundary condition for the geostrophic potential ϕ^1 is a Heaviside function in x and a delta function in z,

$$\phi^1(z=0) = \begin{cases} \phi^1_{max}\delta(z-0) & x > x_{fb}, \\ \phi^1_{min}\delta(z-0) & x < x_{fb}, \end{cases} \tag{3.3a}$$

$$\phi^1(z=1) = \begin{cases} \phi^1_{max}\delta(z-1) & x > x_{fs}, \\ \phi^1_{min}\delta(z-1) & x < x_{fs}. \end{cases} \tag{3.3b}$$

The cross-frontal points where the buoyancy gradient is localized are denoted by x_{fs}, x_{fb} which represent the location of the front nose at the surface (fs) and bottom (fb) of the mixed layer respectively.

The motivation for considering such simplifications is Green's functions theory, as a full flow field solution exists for ϕ^1 and ψ^1 even if only a point source buoyancy gradient is prescribed (e.g. Harnik & Heifetz 2007). An example analytic procedure for finding the first-order solution to (2.26), using delta function approximations and Green's function theory, is given in appendix B.

Figures 9 and 10(m–p) show results for the SQG systems with point source surface conditions. In all forcing cases, the along-front velocity and streamfunction are very similar to the full SQG system solutions in (i–l), especially near the surface.

In conclusion, the SQG geostrophic potential, which contributes most of the along-front velocity, can be reconstructed by surface conditions highly localized near the

front maximum. From a parameterization or numerics development perspective, it is the method of regularizing – or keeping finite – the buoyancy gradient very near the maximum gradient surface expression of the front that will dominate the fidelity of a strain-induced frontal simulation, rather than turbulent fluxes elsewhere or the broad-scale injection of PV.

4. Summary and discussion

In this study, an asymptotic approach estimates the leading-order correction of turbulent fluxes to classic theory for strain-induced frontogenesis. The system described by classic theory may capture the leading-order dynamics, but it is shown here that turbulent fluxes are likely a key secondary component missing in aligning theory with observations and model simulations, especially in the ocean where submesoscale fronts typically coexist with boundary layer turbulence, but also in lower-level atmospheric fronts. Here the effects of turbulent surface and interior fluxes of buoyancy and PV were isolated and examined.

The uncoupled first-order solutions for the along-front geostrophic velocity and ageostrophic overturning streamfunction are obtained by inverting the modified semi-geostrophic frontogenesis equation together with the first non-vanishing-order PV equation. By differentiating between horizontal and vertical eddy viscosity and diffusivity which, in reality, might be associated with parameterizations of mixed layer instabilities, boundary layer turbulence or numerical artefacts as simulated fronts approach singularity, an early understanding of the different impacts of these dissipative operators on fronts is gained. It is found that horizontal viscosity and diffusivity readily act to weaken the front, and thus are key to understanding frontal arrest, consistent with the arresting role of horizontal shear instabilities found by Sullivan & McWilliams ([2018](#)). Vertical viscosity and diffusivity, by contrast, act only to slow strengthening of the front at first, and later vertical diffusivity accelerates frontogenesis resembling turbulent thermal wind theory (McWilliams *et al.* [2015](#); McWilliams [2017](#); Crowe & Taylor [2018](#)).

As the full first-order solution depends on both turbulent boundary conditions and injected interior PV, a decomposition of the results into surface quasi-geostrophic and interior quasi-geostrophic subsystems isolates the contributions to the full solution. In most forcing cases, it is found that SQG dynamics is able to capture most of the along-front velocity and overturning streamfunction features, whereas IQG dynamics has a small contribution. The point source forcing indicates that only a small surface region near the front is needed. In the case of horizontal viscosity, the ageostrophic overturning circulation is only fully reconstructed by including both the SQG and IQG systems. Due to the nature of frontal dynamics, features tend to be localized where the front is strongest. By considering only a point source buoyancy gradient boundary condition, a good approximation to the full SQG response for both the along-front geostrophic velocity and overturning ageostrophic streamfunction was obtained. In a recent paper, Wenegrat *et al.* ([2018](#)) show that boundary layer turbulence can generate a source of PV at the surface, similar in magnitude to PV fluxes from wind and surface buoyancy fluxes (Thomas [2005](#)). It is presently unclear whether our conclusions for the SQG and IQG systems hold true in the presence of strong surface forcing, such as downfront wind forcing, or realistic boundary layer turbulence. However, the same perturbation methods can be used while including wind forcing in ([2.13](#)), and many of the large eddy simulations being analysed include winds.

Furthermore, the asymptotic method presented in this study is derived from the semi-geostrophic equations presented in [HB72](#), implying that the Rossby number is

smaller than 1. However, in the submesoscale regime, both inertial and rotational forces are important and so the Rossby number is $Ro \sim 1$ (e.g. McWilliams 2016). Additionally, semi-geostrophic theory has been shown to be inconsistent with $Ro \sim 1$ (Barkan *et al.* 2019) and curved fronts (Gent, McWilliams & Snyder 1994). The expansion parameter ε is taken to be constant; however, the realistic form is highly uncertain as it represents parameterized effects of turbulent fluxes in the submesoscale regime. The modified theory presented here merely acts as a framework to study the effects of turbulent fluxes during early frontal formation, while the semi-geostrophic assumptions and asymptotic approximation still hold.

It is intended that this framework be utilized in concert with submesoscale simulations with more realistic turbulence parameterizations or resolved turbulence to highlight important regions or aspects of such simulations. At present, large eddy simulations (Moeng 1984; McWilliams, Sullivan & Moeng 1997) are able to resolve the submesoscale dynamics and boundary layer turbulence that motivate this theory. An examination of simulations similar to those studied in Hamlington *et al.* (2014), Smith *et al.* (2016) and Suzuki *et al.* (2016) but including strain-inducing eddies are ongoing. In all runs, a confluent region produces strong frontogenesis, but the cross-frontal scale halts at a finite width. The eventual target is finding quantitative predictions for frontal width, strength and persistence in the presence of realistic turbulent fluxes.

Appendix A. Numerical scheme

A.1. *Parameters*

(i) Dimensionless time (t) range is [0, 19.8] where the zeroth order vanishes according to ST13.
(ii) Dimensionless cross-frontal (x) range is [−2.5, 2.5].
(iii) Dimensionless vertical (z) range is [0, 1].
(iv) $\gamma = 0.1$.
(v) Rossby number $Ro = 0.4$.
(vi) The Froude number is calculated by $Fr = Ro/Bu$ where $Bu = 0.1$ following ST13.

A.2. *First-order solution*

(i) The zeroth-order solution is calculated with (2.22) and (2.23a)–(2.23c), which serve as inputs for the consecutive steps.

(ii) The PV is calculated by integrating the PV evolution equation (2.34) using the forward Euler method for the first three time steps after which the third-order Adam–Bashforth explicit method is used. The zeroth-order solution is used to calculate the advection and and flux terms at every time step.

(iii) In the SQG simulation the PV is taken to be zero.

(iv) The five point stencil method is used to invert, at every time step, the second-order partial differential equation for ϕ^1 (2.30), using inputs from the zeroth-order solution and the PV.

 (v) A similar method is used for ψ (2.26), using inputs from the zeroth-order solution and ϕ^1.

A.3. *Boundary conditions*

For the simulations presented in this paper we do not include fluxes induced by wind shear and thermodynamic forcing.

The boundary conditions for ψ^1 are given by integrating the cross-front momentum equation (2.5a). We use the forward Euler method for the first three time steps after which the third-order Adam–Bashforth explicit method is used. The streamfunction is evaluated at every time step by (2.4). The zeroth-order solution is used as input for the zeroth-order advection and the total flux terms. The first-order advection terms are evaluated at every time step with the explicit method.

The boundary conditions for ϕ^1 are given by integrating the thermodynamic equation (2.5d) by the same method as for ψ^1, where the geostrophic potential is evaluated at every time step by (2.6).

In the IQG simulation the boundary conditions for ϕ^1 are taken to be trivial $\partial \phi^1/\partial z = 0$. In both the IQG and SQG systems we maintain the boundary conditions for ψ^1 since this is the equation for the ageostrophic streamfunction and is independent at each time of the quasi-geostrophic PV inversion. At past times, the Lagrangian history of the boundary conditions does affect ψ_1, ϕ_1, but these historical effects do not directly accumulate in the first-order ageostrophic overturning circulation, which in the perturbation asymptotics, is diagnostically calculated from the zeroth-order fields through (2.26). The nature of this decomposition is highlighted by the characteristics of the boundary conditions in the SQG system, and (2.30) for the IQG system, independent of the first-order Lagrangian derivative. The turbulent flux forcing term $\mathcal{F}(\phi^0)$ in (2.26) is divided into surface and interior domains for the SQG and QG case respectively.

In the point source case, the boundary conditions are calculated by (3.3) where x_{ft}, x_{fb} are the points of maximum along-front velocity on the boundary.

Appendix B. Analytic solution for the delta function approximation

To obtain an analytic framework, we chose the locations for which the zeroth-order solution goes singular as the points of maximum frontogenesis. In this approximation, the point sources of PV $(\hat{q}_{fs}, \hat{q}_{fb})$ can be found by evaluating the PV from (2.34) at these locations.

With the assumption of point sources of PV, ϕ^1 can be found using the Green's function for the PDE (2.30), then (2.26) determines the first-order geostrophic streamfunction ψ^1.

If the PDE is elliptic then we can perform a change of variables so that it becomes $\sim \nabla^2$ in some other coordinate system. We are looking for a change of variables

$(\xi(x, z), \eta(x, z))$ such that $J \equiv \xi_x \eta_z - \xi_z \eta_x \neq 0$ for any x, z in the domain. For an equation of the sort

$$\mathcal{L}[\phi^1] = A\phi^1_{xx} + 2B\phi^1_{xz} + C\phi^1_{zz} = D, \tag{B 1}$$

where

$$\left.\begin{aligned}
A &= Ro^2 \frac{\partial^2 \phi^0}{\partial z^2}, \\
B &= -Ro^2 \frac{\partial^2 \phi^0}{\partial x \partial z}, \\
C &= \left(1 + Ro^2 \frac{\partial^2 \phi^0}{\partial x^2}\right), \\
D &= \hat{q}_{ft}\delta(x - x_{ft})\delta(z - z_{ft}) + \hat{q}_{fb}\delta(x - x_{fb})\delta(z - z_{fb}).
\end{aligned}\right\} \tag{B 2}$$

Assuming A, B, C are real analytic functions in the domain, and that $A(x, y) \neq 0$ (i.e. $\partial b^0/\partial z \neq 0$), a transformation $\Pi(\xi, \eta) = \phi^1(x(\xi, \eta), y(\xi, \eta))$ can be found such that

$$\mathcal{A}\Pi_{\xi\xi} + 2\mathcal{B}\Pi_{\xi\eta} + \mathcal{C}\Pi_{\eta\eta} = \mathcal{D}. \tag{B 3}$$

And

$$\left.\begin{aligned}
\mathcal{A} &= A\xi_x^2 + 2B\xi_x\xi_z + C\xi_z^2, \\
\mathcal{B} &= A\xi_x\eta_x + B(\xi_x\eta_z + \xi_z\eta_x) + C\xi_z\eta_z, \\
\mathcal{C} &= A\eta_x^2 + 2B\eta_x\eta_z + C\eta_z^2.
\end{aligned}\right\} \tag{B 4}$$

Since our operator is elliptic we are looking for ξ, η that satisfy $\mathcal{A} = \mathcal{C}$ and $\mathcal{B} = 0$,

$$A\xi_x^2 + 2B\xi_x\xi_z + C\xi_z^2 = A\eta_x^2 + 2B\eta_x\eta_z + C\eta_z^2, \tag{B 5a}$$

$$A\xi_x\eta_x + B(\xi_x\eta_z + \xi_z\eta_x) + C\xi_z\eta_z = 0. \tag{B 5b}$$

Which can be found by defining the variable $\lambda = \xi + i\eta$, reducing to one equation,

$$A\lambda_x + (B \pm i\sqrt{AC - B^2})\lambda_z = 0, \tag{B 6}$$

where λ is constant on the characteristics (defined on the complex plane)

$$\frac{\mathrm{d}z}{\mathrm{d}x} = \frac{B \pm i\sqrt{AC - B^2}}{A}. \tag{B 7}$$

Inserting the non-dimensional definitions for A, B. C gives

$$\frac{\mathrm{d}z}{\mathrm{d}x} = \frac{-\dfrac{\partial b^0}{\partial x}}{\dfrac{\partial b^0}{\partial z}} \pm i \frac{\sqrt{\left(Ro^2 \dfrac{\partial b^0}{\partial z}\right) \cdot \left(1 + Ro^2 \dfrac{\partial v^0}{\partial x}\right) - \left(Ro^2 \dfrac{\partial b^0}{\partial x}\right)^2}}{\left(Ro^2 \dfrac{\partial b^0}{\partial z}\right)}. \tag{B 8}$$

Integrating the equation with respect to x:

$$\left[z + \int \left(\frac{\partial b^0}{\partial x} \Big/ \frac{\partial b^0}{\partial z} \right) \mathrm{d}x \right] \pm \mathrm{i} \left[\int \frac{\sqrt{\left(Ro^2 \frac{\partial b^0}{\partial z} \right) \cdot \left(1 + Ro^2 \frac{\partial v^0}{\partial x} \right) - \left(Ro^2 \frac{\partial b^0}{\partial x} \right)^2}}{\left(Ro^2 \frac{\partial b^0}{\partial z} \right)} \mathrm{d}x \right]$$

$$= \mathrm{const.} \tag{B 9}$$

This is the characteristic solution for which λ is constant and $\xi = \mathrm{Re}[\lambda]$, $\eta = \mathrm{Im}[\lambda]$

$$\xi = z + \int \left(\frac{\partial b^0}{\partial x} \Big/ \frac{\partial b^0}{\partial z} \right) \mathrm{d}x, \tag{B 10a}$$

$$\eta = \pm \int \frac{\sqrt{\left(Ro^2 \frac{\partial b^0}{\partial z} \right) \cdot \left(1 + Ro^2 \frac{\partial v^0}{\partial x} \right) - \left(Ro^2 \frac{\partial b^0}{\partial x} \right)^2}}{\left(Ro^2 \frac{\partial b^0}{\partial z} \right)} \mathrm{d}x. \tag{B 10b}$$

The problem now reduces to solving the equation in the η, ζ coordinate system, which is a Laplacian operator equal to an equivalent delta function

$$\Pi_{\xi\xi} + \Pi_{\eta\eta} = \frac{\mathcal{D}(\zeta, \eta)}{\mathcal{A}(\zeta, \eta)} \sim \delta(\zeta, \eta). \tag{B 11}$$

Using the definition for ξ, η we can find the boundary conditions on Π from the boundary conditions of ϕ^1.

Since ϕ^1 is confined to the frontal region, it can be assumed that far from the front as $x \to \pm\infty$ the first-order velocities vanish

$$v^1 = \frac{\partial \phi^1}{\partial x} = \frac{\partial \Pi}{\partial \xi} \cdot \frac{\partial \xi}{\partial x} = -\frac{\partial \Pi}{\partial \xi} \cdot \left(\frac{1}{Ro \frac{\partial v^0}{\partial Z}} \right) = -\frac{\partial \Pi}{\partial \xi} \cdot \left(\frac{2}{\mathrm{e}^{\gamma T} Ro^2 B_0'(X)} \right), \tag{B 12}$$

where we use the definition of the slope in X coordinates, as in ST13. The initial buoyancy in X coordinates is $B_0(X) = \frac{1}{2}\mathrm{erf}(X/\sqrt{2}) \to B_0'(X) = (1/\sqrt{2\pi})\mathrm{e}^{-X^2/2}$

$$\to \quad \lim_{x \to \pm\infty} \frac{\partial \Pi}{\partial \xi} = \lim_{x \to \pm\infty} \left[v^1 \Big/ \frac{2\sqrt{2\pi}\mathrm{e}^{X^2/2}}{\mathrm{e}^{\gamma T} Ro^2} \right] = 0. \tag{B 13}$$

Also it can be shown that $\xi \to \pm\infty$ as $X \to \pm\infty$ and $X \to \pm\infty$ as $x \to \pm\infty$. Thus we now have the boundary conditions

$$\lim_{\xi \to \pm\infty} \frac{\partial \Pi}{\partial \xi} = 0. \tag{B 14}$$

In a QG system, we use trivial boundary conditions $\partial b^1 / \partial z = \partial^2 \phi^1 / \partial z^2 = 0$.

$$\frac{\partial \phi^1}{\partial z} = \frac{\partial \Pi}{\partial \eta} \frac{\partial \eta}{\partial z} \quad \rightarrow \quad \frac{\partial^2 \phi^1}{\partial z^2} = \frac{\partial}{\partial z} \left(\frac{\partial \Pi}{\partial \eta} \frac{\partial \eta}{\partial z} \right) = \frac{\partial^2 \Pi}{\partial \eta^2} \left(\frac{\partial \eta}{\partial z} \right)^2 + \frac{\partial \Pi}{\partial \eta} \frac{\partial^2 \eta}{\partial z^2}. \quad \text{(B 15)}$$

In order to obey the boundary conditions, the limit $(\partial^2 \Pi / \partial \eta^2)(\partial \eta / \partial z)^2 \ll (\partial \Pi / \partial \eta)$ $(\partial^2 \eta / \partial z^2)$ implies that

$$0 = \left. \frac{\partial^2 \phi^1}{\partial z^2} \right|_{b.c} = \frac{\partial^2 \Pi}{\partial \eta^2} \left(\frac{\partial \eta}{\partial z} \right)^2 + \frac{\partial \Pi}{\partial \eta} \frac{\partial^2 \eta}{\partial z^2} \approx \left. \frac{\partial \Pi}{\partial \eta} \frac{\partial^2 \eta}{\partial z^2} \right|_{b.c} \quad \rightarrow \quad \left. \frac{\partial \Pi}{\partial \eta} \right|_{b.c} = 0. \quad \text{(B 16)}$$

Thus, it is enough to show that $(\partial \eta / \partial z)^2 \ll \partial^2 \eta / \partial z^2$ and $\partial^2 \Pi / \partial \eta^2 \ll \partial \Pi / \partial \eta$, which are given by the scaling argument

$$[\eta] = \frac{\sqrt{[A][C] - [B]^2}}{[A]} \cdot L = \frac{\sqrt{\dfrac{L^2}{H^2} Ro^2}}{\dfrac{1}{f^2} \dfrac{M^2 L H}{H^2}} \cdot L = Ro^3 \cdot H, \quad \text{(B 17)}$$

$$\rightarrow \quad \left[\left(\frac{\partial \eta}{\partial z} \right)^2 \bigg/ \frac{\partial^2 \eta}{\partial z^2} \right] = \frac{\dfrac{[A][C] - [B]^2}{[A]^2} \cdot \dfrac{L^2}{H^2}}{\dfrac{\sqrt{[A][C] - [B^2]}}{[A]} \cdot \dfrac{L}{H^2}} = \frac{\sqrt{[A][C] - [B]^2}}{[A]} \cdot L. \quad \text{(B 18)}$$

For the HB72 case $Ro \sim O(0.4)$ and $H \sim O(10)$ which means that $Ro^3 \cdot H \sim 10^{-3} \times 10^1 = 10^{-2} \ll 1$. Thus $(\partial \eta / \partial z)^2 \ll \partial^2 \eta / \partial z^2$.

Next, we want to show that $\partial^2 \Pi / \partial \eta^2 \ll \partial \Pi / \partial \eta$

$$\frac{\partial \phi^1}{\partial x} = \begin{cases} \dfrac{\partial \Pi}{\partial \eta} \dfrac{\partial \eta}{\partial x} \\ \dfrac{\partial \Pi}{\partial \xi} \dfrac{\partial \xi}{\partial x} \end{cases} \quad \rightarrow \quad \frac{\partial \Pi}{\partial \eta} \frac{\partial \eta}{\partial x} = \frac{\partial \Pi}{\partial \xi} \frac{\partial \xi}{\partial x} \quad \rightarrow \quad \frac{\partial \Pi}{\partial \eta} = \frac{1}{\dfrac{\partial \eta}{\partial x}} \frac{\partial \Pi}{\partial \xi} \frac{\partial \xi}{\partial x}. \quad \text{(B 19)}$$

In addition, in the same way as we got (B 15) with η, we can do the same with ξ

$$0 = \left. \frac{\partial^2 \phi^1}{\partial z^2} \right|_{b.c} = \frac{\partial^2 \Pi}{\partial \xi^2} \left(\frac{\partial \xi}{\partial z} \right)^2 + \frac{\partial \Pi}{\partial \xi} \frac{\partial^2 \xi}{\partial z^2} \quad \rightarrow \quad \left. \frac{\partial^2 \Pi}{\partial \xi^2} \right|_{b.c} = - \frac{\partial \Pi}{\partial \xi} \frac{\dfrac{\partial^2 \xi}{\partial z^2}}{\left(\dfrac{\partial \xi}{\partial z} \right)^2} \bigg|_{b.c}. \quad \text{(B 20)}$$

Remembering that our initial Laplacian equation for Π is equal to zero everywhere except at the point source. Specifically this means that at the boundaries (assuming the point source is not exactly at the boundary)

$$\frac{\partial^2 \Pi}{\partial \eta^2} + \left. \frac{\partial^2 \Pi}{\partial \xi^2} \right|_{b.c} = 0 \quad \rightarrow \quad \left. \frac{\partial^2 \Pi}{\partial \eta^2} \right|_{b.c} = - \left. \frac{\partial^2 \Pi}{\partial \xi^2} \right|_{b.c} = \frac{\partial \Pi}{\partial \xi} \frac{\dfrac{\partial^2 \xi}{\partial z^2}}{\left(\dfrac{\partial \xi}{\partial z} \right)^2} \bigg|_{b.c}. \quad \text{(B 21)}$$

Now comparing $\partial^2 \Pi / \partial \eta^2$, $\partial \Pi / \partial \eta$ by using the expressions found for each on the boundaries and the scaling of the problem

$$\left[\frac{\partial^2 \Pi}{\partial \eta^2} \Big/ \frac{\partial \Pi}{\partial \eta} \right] = \left[\frac{\partial \eta}{\partial x} \frac{\partial^2 \xi}{\partial z^2} \right] \Big/ \left[\frac{\partial \xi}{\partial x} \left(\frac{\partial \xi}{\partial z} \right)^2 \right] = \frac{\dfrac{[\eta]}{L} \dfrac{[\xi]}{H^2}}{\dfrac{[\xi]}{L} \dfrac{[\xi]^2}{H^2}} = \frac{[\eta]}{[\xi]^2}$$

$$= \frac{\dfrac{\sqrt{AC - B^2}}{A} L}{\left(H + \dfrac{B}{A} L \right)^2} = \frac{1}{4RoH} \sim \frac{1}{1.6H} \ll 1. \tag{B 22}$$

Thus also $\partial^2 \Pi / \partial \eta^2 \ll \partial \Pi / \partial \eta$ which means that $\partial^2 \Pi / \partial \eta^2 \, (\partial \eta / \partial z)^2 \ll (\partial \Pi / \partial \eta)$ $(\partial^2 \eta / \partial z^2)$.

It can be shown that $\eta \to \infty$ as $z \to -\infty$ and we can define $\eta = \eta_0$ for $z = 0$.

Thus we now have the second boundary conditions

$$\lim_{\eta \to \infty, \eta_0} \frac{\partial \Pi}{\partial \eta} = 0. \tag{B 23}$$

Now we can use Green's functions theory to solve this equation with von Neumann boundary conditions on a half-plane

$$\lim_{\xi \to \pm \infty} \frac{\partial \Pi}{\partial \xi} = 0, \tag{B 24a}$$

$$\lim_{\eta \to \infty, \eta_0} \frac{\partial \Pi}{\partial \eta} = 0. \tag{B 24b}$$

A similar argument can be made for the SQG case with the point source being located on the boundary.

We can solve a linear PDE with an operator $\mathcal{L}$ using the following method:

$$\mathcal{L}\{\Pi\} = F(\eta, \xi) \sim \hat{q}(t) \delta(\eta - p, \xi - s). \tag{B 25}$$

We are looking for

$$\mathcal{L}\{G(\eta, \xi; p, s)\} = \delta(\eta - p, \xi - s). \tag{B 26}$$

Multiplying by $F(p, s)$ and integrating by p, s

$$\int \mathcal{L}\{G(\eta, \xi; \, p, s)\} F(p, s) \, \mathrm{d}p \, \mathrm{d}s = \int \delta(\eta - p, \xi - s) F(p, s) \, \mathrm{d}p \, \mathrm{d}s = F(\eta, \xi). \tag{B 27}$$

Since $\mathcal{L}$ is a linear operator, acting on (η, ξ) we can take it out of the integral which acts on (p, s)

$$\mathcal{L}\{\Pi\} = F(\eta, \xi) = \int \mathcal{L}\{G(\eta, \xi; p, s)\} F(p, s) \, \mathrm{d}p \, \mathrm{d}s = \mathcal{L}\left[\int G(\eta, \xi; p, s) F(p, s) \, \mathrm{d}p \, \mathrm{d}s \right]. \tag{B 28}$$

Thus the solution for $\Pi(\eta, \xi)$ is given by

$$\Pi(\eta, \xi) = \int G(\eta, \xi; p, s) F(p, s) \, \mathrm{d}p \, \mathrm{d}s. \tag{B 29}$$

Since $F(\eta, \xi) \sim \hat{q}(t) \delta(\eta - p, \xi - s)$, the Green's function is proportional to the function $\to \Pi \sim G$.

We are looking for a solution matching two point sources on a half-plane with homogeneous von Neumann boundary conditions. This means we need to use the method of images in order to find the appropriate solution. In order to satisfy the boundary condition $\partial \Pi / \partial \eta|_{\eta = \eta_0} = 0$, we need to add two image point sources of the same magnitude, sign and distance from the boundary as the point sources located at the front.

The Green's function matching von Neumann boundary conditions is

$$G(\xi, \eta; \xi', \eta') = -\frac{1}{4\pi} \frac{1}{\sqrt{(\xi - \xi')^2 + (\eta - \eta')^2}}. \tag{B 30}$$

In our problem each point source is multiplied by a factor of $\mathcal{D}(\xi_f, \eta_f, t)/\mathcal{A}(\xi_f, \eta_f, t)$, so the total Green's function, which is also the solution for Π, is

$$\Pi(\xi, \eta) = -\frac{1}{4\pi} \frac{\hat{q}_{ft}}{\mathcal{A}_{ft}} \frac{1}{\sqrt{(\xi - \xi_{ft})^2 + (\eta - \eta_{ft})^2}} - \frac{1}{4\pi} \frac{\hat{q}_{ft}}{\mathcal{A}_{ft}} \frac{1}{\sqrt{(\xi - \xi_{ft})^2 + (\eta + \eta_{ft})^2}}$$
$$- \frac{1}{4\pi} \frac{\hat{q}_{fb}}{\mathcal{A}_{fb}} \frac{1}{\sqrt{(\xi - \xi_{fb})^2 + (\eta - \eta_{fb})^2}} - \frac{1}{4\pi} \frac{\hat{q}_{fb}}{\mathcal{A}_{fb}} \frac{1}{\sqrt{(\xi - \xi_{fb})^2 + (\eta + \eta_{fb})^2}}. \tag{B 31}$$

This is the solution for the first-order geostrophic potential ϕ^1 in ξ, η space.

REFERENCES

BACHMAN, S. D., FOX-KEMPER, B. & BRYAN, F. O. 2015 A tracer-based inversion method for diagnosing eddy-induced diffusivity and advection. *Ocean Model.* **86**, 1–14.

BACHMAN, S. D., FOX-KEMPER, B., TAYLOR, J. R. & THOMAS, L. N. 2017 Parameterization of frontal symmetric instabilities. Part I. Theory for resolved fronts. *Ocean Model.* **109**, 72–95.

BARCILON, V. 1998 On the barotropic ocean with bottom friction. *J. Mar. Res.* **56** (4), 731–771.

BARKAN, R., MOLEMAKER, J. M., SRINIVASAN, K., MCWILLIAMS, J. C. & D'ASARO, E. A. 2019 The role of horizontal divergence in submesoscale frontogenesis. *J. Phys. Oceanogr* **49** (6), 1593–1618.

BENDER, C. M. & ORSZAG, S. A. 2013 *Advanced Mathematical Methods for Scientists and Engineers I: Asymptotic Methods and Perturbation Theory*. Springer Science & Business Media.

BENTHUYSEN, J. & THOMAS, L. N. 2012 Friction and diapycnal mixing at a slope: boundary control of potential vorticity. *J. Phys. Oceanogr.* **42** (9), 1509–1523.

BLUMEN, W. 1978 Uniform potential vorticity flow. Part I. Theory of wave interactions and two-dimensional turbulence. *J. Atmos. Sci.* **35** (5), 774–783.

BOND, N. A. & FLEAGLE, R. G. 1985 Structure of a cold front over the ocean. *Q. J. R. Meteorol. Soc.* **111** (469), 739–759.

BOUTLE, I. A., BELCHER, S. E. & PLANT, R. S. 2015 Friction in mid-latitude cyclones: an Ekman-PV mechanism. *Atmos. Sci. Lett.* **16** (2), 103–109.

BRETHERTON, F. P. 1966 Critical layer instability in baroclinic flows. *Q. J. R. Meteorol. Soc.* **92** (393), 325–334.

CALLIES, J., FLIERL, G., FERRARI, R. & FOX-KEMPER, B. 2016 The role of mixed-layer instabilities in submesoscale turbulence. *J. Fluid Mech.* **788**, 5–41.

CAPET, X., KLEIN, P., HUA, B. L., LAPEYRE, G. & MCWILLIAMS, J. C. 2008a Surface kinetic energy transfer in surface quasi-geostrophic flows. *J. Fluid Mech.* **604**, 165–174.

CAPET, X., MCWILLIAMS, J. C., MOLEMAKER, J. M. & SHCHEPETKIN, A. F. 2008b Mesoscale to submesoscale transition in the California current system. Part I. Flow structure, eddy flux, and observational tests. *J. Phys. Oceanogr.* **38** (1), 29–43.

CAPET, X., ROULLET, G., KLEIN, P. & MAZE, G. 2016 Intensification of upper-ocean submesoscale turbulence through Charney baroclinic instability. *J. Phys. Oceanogr.* **46** (11), 3365–3384.

CHARNEY, J. G. 1971 Geostrophic turbulence. *J. Atmos. Sci.* **28** (6), 1087–1095.

CHAVANNE, C. P. & KLEIN, P. 2016 Quasigeostrophic diagnosis of mixed layer dynamics embedded in a mesoscale turbulent field. *J. Phys. Oceanogr.* **46** (1), 275–287.

COOPER, I. M., THORPE, A. J. & BISHOP, C. H. 1992 The role of diffusive effects on potential vorticity in fronts. *Q. J. R. Meteorol. Soc.* **118** (506), 629–647.

CROWE, M. N. & TAYLOR, J. R. 2018 The evolution of a front in turbulent thermal wind balance. Part 1. Theory. *J. Fluid Mech.* **850**, 179–211.

DIJKSTRA, H. A. & MOLEMAKER, J. M. 1997 Symmetry breaking and overturning oscillations in thermohaline-driven flows. *J. Fluid Mech.* **331**, 169–198.

EADY, E. T. 1949 Long waves and cyclone waves. *Tellus* **1** (3), 33–52.

FERRARI, R. & WUNSCH, C. 2009 Ocean circulation kinetic energy: reservoirs, sources, and sinks. *Annu. Rev. Fluid Mech.* **41**, 253–282.

FOX-KEMPER, B., DANABASOGLU, G., FERRARI, R., GRIFFIES, S. M., HALLBERG, R. W., HOLLAND, M. M., MALTRUD, M. E., PEACOCK, S. & SAMUELS, B. L. 2011 Parameterization of mixed layer eddies. Part III. Implementation and impact in global ocean climate simulations. *Ocean Model.* **39**, 61–78.

FOX-KEMPER, B. & FERRARI, R. 2009 An eddifying Parsons model. *J. Phys. Oceanogr.* **39** (12), 3216–3227.

FOX-KEMPER, B., FERRARI, R. & HALLBERG, R. W. 2008 Parameterization of mixed layer eddies. Part I. Theory and diagnosis. *J. Phys. Oceanogr.* **38** (6), 1145–1165.

GENT, P. R., MCWILLIAMS, J. C. & SNYDER, C. 1994 Scaling analysis of curved fronts. Validity of the balance equations and semigeostrophy. *J. Atmos. Sci.* **51** (1), 160–163.

GILL, A. E. 1982 *Atmosphere-Ocean Dynamics (International Geophysics Series)*. Academic Press.

GRIFFIES, S. M. 1998 The Gent–McWilliams skew flux. *J. Phys. Oceanogr.* **28** (5), 831–841.

HÅKANSSON, M. 2002 A two-dimensional numerical study of effects of vertical diffusion in frontal zones. *Q. J. R. Meteorol. Soc.* **128** (585), 2439–2467.

HAMLINGTON, P. E., VAN ROEKEL, L. P., FOX-KEMPER, B., JULIEN, K. & CHINI, G. P. 2014 Langmuir–submesoscale interactions: descriptive analysis of multiscale frontal spindown simulations. *J. Phys. Oceanogr.* **44** (9), 2249–2272.

HARNIK, N. & HEIFETZ, E. 2007 Relating overreflection and wave geometry to the counterpropagating Rossby wave perspective: toward a deeper mechanistic understanding of shear instability. *J. Atmos. Sci.* **64** (7), 2238–2261.

HAYNES, P. H. & MCINTYRE, M. E. 1987 On the evolution of vorticity and potential vorticity in the presence of diabatic heating and frictional or other forces. *J. Atmos. Sci.* **44** (5), 828–841.

HOSKINS, B. J. 1975 The geostrophic momentum approximation and the semi-geostrophic equations. *J. Atmos. Sci.* **32** (2), 233–242.

HOSKINS, B. J. 1982 The mathematical theory of frontogenesis. *Annu. Rev. Fluid Mech.* **14** (1), 131–151.

HOSKINS, B. J. 1991 Towards a PV-θ view of the general circulation. *Tellus* **43** (4), 27–36.

HOSKINS, B. J. & BRETHERTON, F. P. 1972 Atmospheric frontogenesis models: mathematical formulation and solution. *J. Atmos. Sci.* **29** (1), 11–37.

HOSKINS, B. J., MCINTYRE, M. E. & ROBERTSON, A. W. 1985 On the use and significance of isentropic potential vorticity maps. *Q. J. R. Meteorol. Soc.* **111** (470), 877–946.

KLEIN, P., LAPEYRE, G., ROULLET, G., LE GENTIL, S. & SASAKI, H. 2011 Ocean turbulence at meso and submesoscales: connection between surface and interior dynamics. *Geophys. Astrophys. Fluid Dyn.* **105** (4–5), 421–437.

KURGANSKY, M. V. & PISNICHENKO, I. A. 2000 Modified ertels potential vorticity as a climate variable. *J. Atmos. Sci.* **57** (6), 822–835.

LACASCE, J. H. & MAHADEVAN, A. 2006 Estimating subsurface horizontal and vertical velocities from sea-surface temperature. *J. Mar. Res.* **64** (5), 695–721.

LACASCE, J. H. & WANG, J. 2015 Estimating subsurface velocities from surface fields with idealized stratification. *J. Phys. Oceanogr.* **45** (9), 2424–2435.

LAPEYRE, G. & KLEIN, P. 2006 Dynamics of the upper oceanic layers in terms of surface quasigeostrophy theory. *J. Phys. Oceanogr.* **36** (2), 165–176.

LAPEYRE, G., KLEIN, P. & HUA, B. L. 2006 Oceanic restratification forced by surface frontogenesis. *J. Phys. Oceanogr.* **36** (8), 1577–1590.

LARGE, W. G., MCWILLIAMS, J. C. & DONEY, S. C. 1994 Oceanic vertical mixing: a review and a model with a nonlocal boundary layer parameterization. *Rev. Geophys.* **32** (4), 363–403.

LI, Q., REICHL, B. G., FOX-KEMPER, B., ADCROFT, A. J., BELCHER, S., DANABASOGLU, G., GRANT, A., GRIFFIES, S. M., HALLBERG, R. W., HARA, T. *et al.* 2019 Comparing ocean boundary vertical mixing schemes including Langmuir turbulence. *J. Adv. Model. Earth Syst. (JAMES)* (in press).

MAHADEVAN, A. 2016 The impact of submesoscale physics on primary productivity of plankton. *Annu. Rev. Mar. Sci.* **8**, 161–184.

MAHADEVAN, A. & ARCHER, D. 2000 Modeling the impact of fronts and mesoscale circulation on the nutrient supply and biogeochemistry of the upper ocean. *J. Geophys. Res.* **105** (C1), 1209–1225.

MARSHALL, J. C. & NURSER, A. G. 1992 Fluid dynamics of oceanic thermocline ventilation. *J. Phys. Oceanogr.* **22** (6), 583–595.

MCWILLIAMS, J. C. 2016 Submesoscale currents in the ocean. *Proc. R. Soc.* A **472**, 20160117.

MCWILLIAMS, J. C. 2017 Submesoscale surface fronts and filaments: secondary circulation, buoyancy flux, and frontogenesis. *J. Fluid Mech.* **823**, 391–432.

MCWILLIAMS, J. C., GULA, J., MOLEMAKER, J. M., RENAULT, L. & SHCHEPETKIN, A. F. 2015 Filament frontogenesis by boundary layer turbulence. *J. Phys. Oceanogr.* **45** (8), 1988–2005.

MCWILLIAMS, J. C., MOLEMAKER, M. & OLAFSDOTTIR, E. 2009 Linear fluctuation growth during frontogenesis. *J. Phys. Oceanogr.* **39** (12), 3111–3129.

MCWILLIAMS, J. C., SULLIVAN, P. P. & MOENG, C.-H. 1997 Langmuir turbulence in the ocean. *J. Fluid Mech.* **334**, 1–30.

MOENG, C.-H. 1984 A large-eddy-simulation model for the study of planetary boundary-layer turbulence. *J. Atmos. Sci.* **41** (13), 2052–2062.

MOLEMAKER, J. M., MCWILLIAMS, J. C. & CAPET, X. 2010 Balanced and unbalanced routes to dissipation in an equilibrated Eady flow. *J. Fluid Mech.* **654**, 35–63.

NAGAI, T., TANDON, A. & RUDNICK, D. L. 2006 Two-dimensional ageostrophic secondary circulation at ocean fronts due to vertical mixing and large-scale deformation. *J. Geophys. Res.* **111**, C09038.

NAKAMURA, N. 1994 Nonlinear equilibration of two-dimensional Eady waves: simulations with viscous geostrophic momentum equations. *J. Atmos. Sci.* **51** (7), 1023–1035.

NAKAMURA, N. & HELD, I. M. 1989 Nonlinear equilibration of two-dimensional Eady waves. *J. Atmos. Sci.* **46** (19), 3055–3064.

OLITA, A., CAPET, A., CLARET, M., MAHADEVAN, A., POULAIN, P. M., RIBOTTI, A., RUIZ, S., TINTORÉ, J., TOVAR-SÁNCHEZ, A. & PASCUAL, A. 2017 Frontal dynamics boost primary production in the summer stratified Mediterranean sea. *Ocean Dyn.* **67** (6), 767–782.

PARSONS, A. T. 1969 A two-layer model of Gulf Stream separation. *J. Fluid Mech.* **39** (3), 511–528.

PEARSON, B. & FOX-KEMPER, B. 2018 Log-normal turbulence dissipation in global ocean models. *Phys. Rev. Lett.* **120** (9), 094501.

PEDLOSKY, J. 1982 *Geophysical Fluid Mechanics*. Springer.

PHAM, H. T. & SARKAR, S. 2018 Ageostrophic secondary circulation at a submesoscale front and the formation of gravity currents. *J. Phys. Oceanogr.* **48** (10), 2507–2529.

POLLARD, R. T. & REGIER, L. A. 1992 Vorticity and vertical circulation at an ocean front. *J. Phys. Oceanogr.* **22** (6), 609–625.

RENAULT, L., MCWILLIAMS, J. C. & GULA, J. 2018 Dampening of submesoscale currents by air–sea stress coupling in the californian upwelling system. *Sci. Rep.* **8** (1), 13388.

RHINES, P. B. 1986 Vorticity dynamics of the oceanic general circulation. *Annu. Rev. Fluid Mech.* **18** (1), 433–497.

ROTUNNO, R., SKAMAROCK, W. C. & SNYDER, C. 1994 An analysis of frontogenesis in numerical simulations of baroclinic waves. *J. Atmos. Sci.* **51** (23), 3373–3398.

SALMON, R. 1998 *Lectures on Geophysical Fluid Dynamics*. Oxford University Press.

SHAKESPEARE, C. J. & TAYLOR, J. R. 2013 A generalized mathematical model of geostrophic adjustment and frontogenesis: uniform potential vorticity. *J. Fluid Mech.* **736**, 366–413.

SIEDLER, G., GRIFFIES, S. M., GOULD, J. & CHURCH, J. 2013 *Ocean Circulation and Climate: A 21st Century Perspective*. Academic Press.

SMITH, K. M., HAMLINGTON, P. E. & FOX-KEMPER, B. 2016 Effects of submesoscale turbulence on ocean tracers. *J. Geophys. Res.* **121** (1), 908–933.

STAMPER, M. A., TAYLOR, J. R. & FOX-KEMPER, B. 2018 The growth and saturation of submesoscale instabilities in the presence of a barotropic jet. *J. Phys. Oceanogr* **48** (11), 2779–2797.

SULLIVAN, P. P. & MCWILLIAMS, J. C. 2018 Frontogenesis and frontal arrest of a dense filament in the oceanic surface boundary layer. *J. Fluid Mech.* **837**, 341–380.

SUZUKI, N., FOX-KEMPER, B., HAMLINGTON, P. E. & VAN ROEKEL, L. P. 2016 Surface waves affect frontogenesis. *J. Geophys. Res.* **121** (5), 3597–3624; Gulf Oil Spill special section.

TAYLOR, J. R. & FERRARI, R. 2011 Ocean fronts trigger high latitude phytoplankton blooms. *Geophys. Res. Lett.* **38**, L23601.

THOMAS, L. N. 2005 Destruction of potential vorticity by winds. *J. Phys. Oceanogr.* **35** (12), 2457–2466.

THOMAS, L. N. & FERRARI, R. 2008 Friction, frontogenesis, and the stratification of the surface mixed layer. *J. Phys. Oceanogr.* **38** (11), 2501–2518.

THOMPSON, L. 2000 Ekman layers and two-dimensional frontogenesis in the upper ocean. *J. Geophys. Res.* **105** (C3), 6437–6451.

TWIGG, R. D. & BANNON, P. R. 1998 Frontal equilibration by frictional processes. *J. Atmos. Sci.* **55** (6), 1084–1087.

WENEGRAT, J. O., THOMAS, L. N., GULA, J. & MCWILLIAMS, J. C. 2018 Effects of the submesoscale on the potential vorticity budget of ocean mode waters. *J. Phys. Oceanogr.* **48** (9), 2141–2165.

XU, Q., GU, W. & GAO, J. 1998 Baroclinic Eady wave and fronts. Part I. Viscous semigeostrophy and the impact of boundary condition. *J. Atmos. Sci.* **55** (24), 3598–3615.